AFIT/GSO/ENP/93D-01

PERFORMANCE IMPACTS OF ACTUATOR MISALIGNMENTS AND FAILURES IN LARGE-APERTURE ADAPTIVE-OPTIC TELESCOPES

THESIS

Presented to the Faculty of the Graduate School of Engineering

of the Air Force Institute of Technology

Air University

In Partial Fulfillment of the

Requirements for the Degree of

Master of Science in Space Operations

Timothy D. Hogan, B.S.

Captain, USAF

DECEMBER, 1993

ACKNOWLEDGEMENTS

This thesis is dedicated to the memory of my mother, Martha Louise Slaughter, my first and favorite teacher. She instilled in me the desire to learn, achieve, and succeed. I could never thank her enough for all she and my dad, William D. Slaughter, taught me through the years. Along with great parents, the Lord has blessed me with a wonderful wife and children. We learned together what it means for the whole family to be assigned to AFIT. I never would have made it without Mary Ann and her consistent understanding support. It is thanks to her that my daughters still know who I am. Kelly Ann and Melissa will never know how much they helped me just by running to the door and yelling my favorite name, "Daddy!" Thanks to you all!

Many other people have helped me throughout this thesis process. I wish to thank my classmates in GSO-93D for their support in all of the classes we suffered through together. Also, Lt Col T. S. Kelso for passing on such a strong vision of the GSO program, as well as the Air Force's space mission. I want to thank Lt Col Kelso and Dr. Byron Welsh for supporting me as committee members along with my advisor, Capt Mike Roggemann, for their faith in my abilities to handle a thesis in a field I knew virtually nothing about. Thank you for your patience, insight, teaching, and the occasional two by four over the head (some day I may actually understand what mean-square-residual phase error is and where the hyphens belong).

Finally, I praise my Lord Jesus Christ for this experience and all that He has taught me in the last eighteen months. It was by His grace that I made it. Thank-you for my family and friends and all that you provide for us.

Timothy D. Hogan

TABLE OF CONTENTS

Page

List of Figures

List of Tables

ABSTRACT

Large-aperture telescopes require adaptive optics in order to compensate for atmospheric turbulence which would otherwise negate the resolution advantages of using large apertures. This investigation analyzes the impacts of misalignments and failures, in the deformable mirror actuators, upon the performance of such systems. A numerical simulation of a standard adaptive optics system is used to generate characteristic optical transfer function (OTF) and signal-to-noise ratio (SNR) performance metrics. The performance impacts of the misalignments are shown to be dependent upon the Fried parameter (effective telescope diameter), the source object brightness, and the control system time delay. The degree of performance degradation is directly related to the relative value of the Fried parameter to the deformable mirror displacement (misalignment cases) and the effective actuator spacing (actuator failure cases). The results indicate that the impact of misalignments and failures is small when seeing conditions are good or the percentage misalignments and failures are small.

I. INTRODUCTION

Background

Adaptive Optics.

Atmospheric turbulence is a major problem in optical astronomy since it drastically reduces the angular resolution of telescopes. This turbulence causes random variations in the index of refraction of the optical path which results in random phase aberrations at the telescope. These aberrations produce a distorted image in the image plane of the telescope. For small-aperture systems, the image will appear to have a random motion, which causes stars to appear to twinkle. For large-aperture telescopes, the image spreads or blurs. Thus, the atmospheric conditions, rather than aperture size and telescope design, determine the limiting resolution of the imaging system (6:283) (8:451).

These effects become significant design considerations for large telescopes. Unless the atmospheric effects are counteracted by image-compensation techniques, a large telescope (e.g., 4-meter class) will have the effective resolution of a small aperture telescope (e.g., 10-cm class). With this in mind, adaptive optics have been proposed to compensate for the atmospheric aberrations (4:651).

Advanced Electro-Optical System (AEOS).

The Air Force Maui Optical Station (AMOS) has been a major contributor to the U.S. Space Surveillance Network (SSN) as the only site capable of providing optical images of low-earth-orbiting satellites. AMOS is a major contributor to Department of Defense (DoD) research and development of advanced electro-optical systems and capabilities. The Air Force's Phillips Laboratory has demonstrated the feasibility of atmospheric compensation using adaptive optics on the current 1.6-meter telescope at AMOS (10:7433). In support of new operational mission requirements, the Advanced

Electro-Optical System (AEOS) program office is designing and acquiring a new 4-meter telescope for the Maui site which will require a more complex adaptive optics system than designed to date.

This thesis provides the basis for understanding the effects of certain design and operational parameters on system performance of large-aperture adaptive-optic telescopes. The performance impacts of misalignment and failure of deformable mirror actuators are analyzed. This characterization of system performance as a function of object, environment, and telescope parameters, will allow the AEOS program office to determine how these parameters impact the design and operational specifications for the system. The expected effects of possible misalignments and failures will impact design specifications, scheduled maintenance, and anticipated replacement of the deformable mirror.

Problem Statement

This thesis investigates design and operational parameters of adaptive optics (AO) systems used for large-aperture telescopes. The effects of misalignment and partial failure of the deformable mirror (DM) actuators are analyzed to determine their impact upon design specifications as well as operational performance. Overall system performance is analyzed relative to telescope, environmental, and object characteristics. Design recommendations are made for AEOS which are applicable to any large aperture telescope system using adaptive optics.

Literature Review

This section presents a review of the current and proposed adaptive optics systems for large telescopes based upon current literature in the field. Reviewed topics include:

1. Methods of atmospheric compensation

2. Models used to simulate atmospheric turbulence and compensation
3. Performance metrics used to evaluate system performance

The review focuses on systems and analysis applicable to the design of large-aperture telescopes.

Methods of Atmospheric Compensation.

Three methods of atmospheric compensation have been proposed in the literature: *speckle imaging, adaptive optics,* and *hybrid methods.* Speckle imaging is a form of post-detection compensation which attempts to reconstruct an image of the object from short exposure images formed by the telescope (6:283). Adaptive optics (AO) is a form of pre-detection compensation which attempts to remove the random phase aberrations before the image is formed by the telescope. Hybrid methods combine the pre-detection and post-detection techniques, capitalizing on the trade-offs of each (7:4227). This review concentrates upon adaptive optics techniques applicable to AEOS.

Adaptive Optics.

Adaptive optics are, by nature, active and real-time systems. Adaptive optics systems correct for the atmospheric distortion by applying an estimate of the complex conjugate phase of the distortion to the incoming wavefront while imaging is proceeding. In an ideal system, the application of the conjugate cancels the phase distortion in the wavefront. As an example of a standard AO system, Figure 1-1 shows the wavefront sensing and compensation system for the AMOS 1.6-meter telescope.

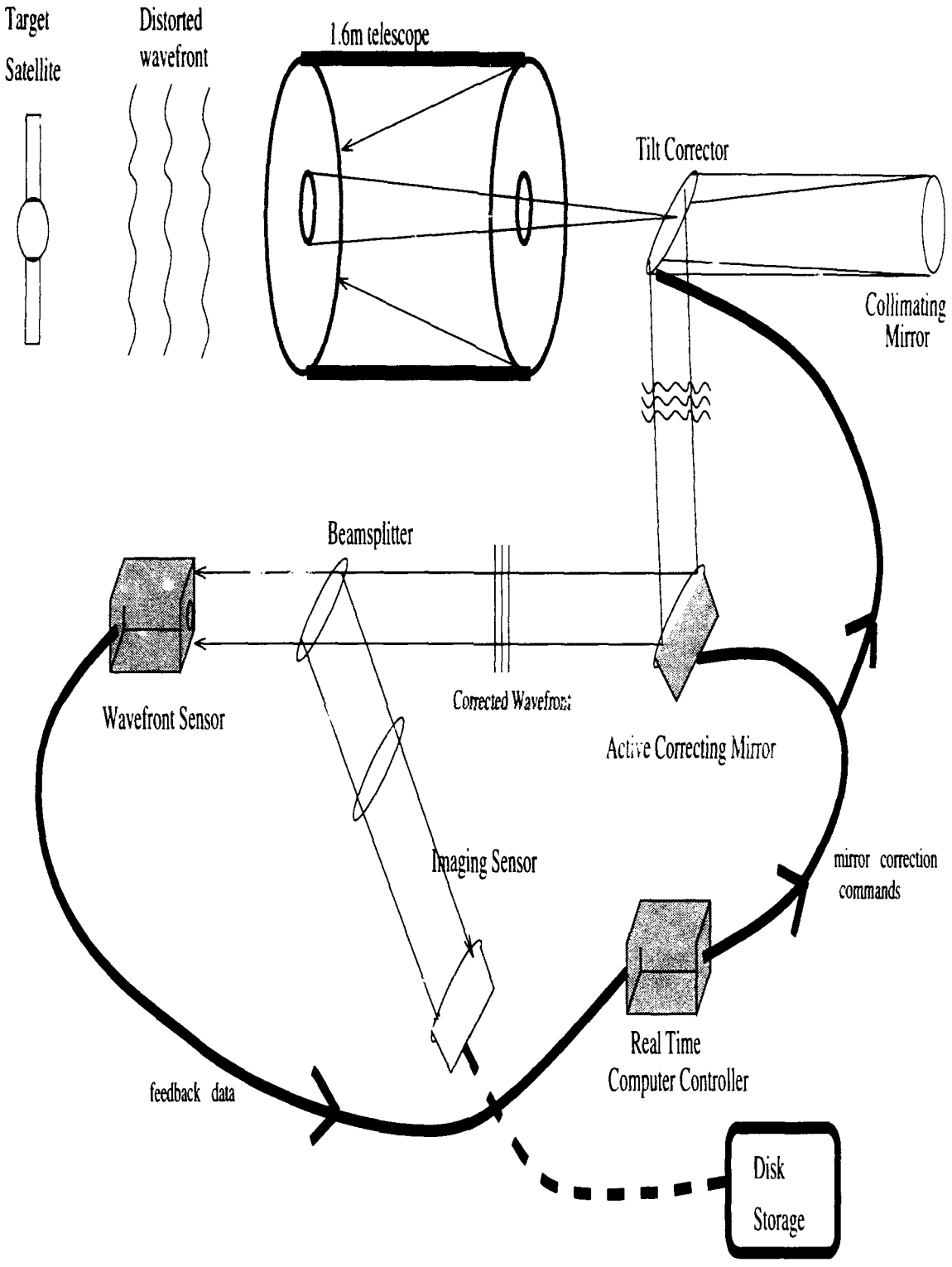

Figure 1-1 AMOS Adaptive Optics System (10:7433)

A standard system consists of the following main components:

- Wavefront sensor to measure the incoming wavefront phase
- Reconstruction algorithm and control law to calculate correction commands
- Deformable mirror with actuators to apply the correction commands.

The wavefront sensor (WFS) estimates the instantaneous state (wavefront phases) of the generalized pupil function. The deformable mirror (DM), connected to the WFS through a control law, applies an estimate of the conjugate of the phase of the generalized pupil function to the propagating wave prior to detection (7:4227). Published schemes for adaptive optics typically use dense arrays of WFS subapertures to measure the wavefront distortion and dense arrays of DM actuators to apply the appropriate correction (7:4227) (8:451)(10:7433)(12:1913).

A *fully-compensated* adaptive optics system uses a deformable mirror with actuators spaced equal to the Fried atmospheric coherence length, r_0 (effective diameter of telescope imposed by atmospheric distortion). Systems with fewer actuators, spaced farther than the r_0 value, are referred to as *partially-compensated.* Typical values for r_0 range from 5-12 cm for the Maui site. Theoretically, fully compensated systems can compensate to near diffraction-limited performance. The large number of components required for full compensation on large telescopes leads to technical difficulties inherent to operational systems with many active components. The maintenance, as well as reliability, of such systems make them practical only in large-aperture telescopes where. While the performance gains achievable with fully-compensated systems justifies their use with large telescopes, partially-compensated systems offer significant performance gains with less operational problems. The utility of using partial compensation was demonstrated by showing that partially-compensated systems can achieve much improved performance over uncompensated systems and do so with much less complexity and cost (5:2249).

This result leads to the hybrid configuration. The utility of this approach has been demonstrated by trading image reconstruction for full pre-detection compensation (7:4227). Comparing the performance of the full compensation case with cases of reduced actuators and using image reconstruction to boost the signal-to-noise ratio (SNR) of the reduced actuator cases shows that there is recoverable high frequency information in the partial-compensation case. By using image reconstruction to recover this information, near-diffraction-limited performance can be obtained without the expense of full-compensation adaptive optics.

Atmospheric Models.

Kolmogorov's work on energy transfer in turbulent flows is the basis for models of the turbulent atmosphere (6:285). It is the basis for modeling the seeing conditions of the atmosphere as a random stochastic process dependent upon the altitude, temperature, and humidity. A computer simulation which models an adaptive optics system, including simulation of turbulent atmosphere effects, has been used previously (8:459)(9:2000). The effects are modeled as a random-turbulence-induced phase screen in the pupil of the telescope. The technique is based upon an analytical method which produces a structure function equal to the theoretical prediction (8:460).

Adaptive Optics Models.

An analytical method for generating and correcting wavefronts has been used to analyze partial-compensation systems. Comparison of the partially corrected and uncorrected models to the diffraction-limited model using representations of images calculated from the averaged optical transfer function (OTF) demonstrate the substantial seeing improvement obtainable with an adaptive optics system with a limited number of actuators (5:2251).

The performance of adaptive optics systems which use wavefront phase-slope measurements to estimate the distorted wavefronts has been investigated using a standard

AO model to derive analytical expressions for the performance metrics: OTF, point spread function (PSF), and Strehl ratio (11:1771). The model allows the use of these metrics to analyze system performance relative to variations in wavefront measurement photon noise, wavefront sensor spacing, and actuator spacing (12:1913).

Computer Simulation.

Numerical simulations allow investigations into the performance of various systems which are not tractable analytically (8:459). Additionally, simulations have been used to produce images of an object with the effects of turbulence and wavefront correction considered. The steps in such a simulation program are outlined below:

The first step sets up:

- The wavefront reconstruction matrix (control law),
- The phase screen generator (turbulence effects),
- Templates for the telescope pupil and wavefront subapertures (telescope configuration), and
- The optimal positions of the deformable mirror actuators (active optical element).

The main iteration process calculates:

- A realization of a random-turbulence-induced phase screen in the pupil of the telescope,
- Wavefront sensor measurements,
- Actuator commands based upon the reconstruction control law,
- Effect of the actuators' response upon a future wavefront (open-loop design), and
- The single-frame-residual phase error and instantaneous optical transfer function (OTF).

The iteration portion is performed for a statistically meaningful number of independent realizations of the phase distortions and correction, typically on the order of a few hundred. The model accumulates and averages the single-frame-residual phase errors as well as OTFs to produce a mean-square-residual phase error, along with the mean and variance for the overall OTF produced by averaging multiple image frames. The signal-to-noise ratio (SNR) can be calculated using the statistical representations of the overall

OTF. This simulation was used to evaluate the performance of two different wavefront reconstructors and show that the minimum-variance reconstructor is superior to the least-squares reconstructor based upon the average imaging SNR as a function of spatial frequency (8:464).

An important element of these models is the modeling of the correlations between the wavefront sensing, estimation, and correction instead of treating them as independent operations. These correlations are very important in the analytical analysis, as well as the numerical simulations. Performance metrics are used to quantify and compare the performance of differing systems.

Performance Metrics and Optimization.

The designs of adaptive optics systems are analyzed and optimized based upon a variety of performance measures. This section summarizes some of the performance metrics presented in the reviewed paper. Researchers have analyzed individual components, as well as overall systems, using a variety of measures.

Mean-Square-Residual Phase Error.

A system of wavefront sensing and correction has been used to derive the mean-square-residual error as a performance measure. This is simply a measure of the mean-square difference between the corrected wavefront and a planar wavefront. An optimum system minimizes the error by properly weighting the reconstruction matrix which determines the influence of each individual actuator on the deformable mirror (11:1772).

Optical Transfer Function (OTF) and Strehl Ratio.

The OTF and the mean-square error have been used, along with the point spread function (PSF) and Strehl ratio, as measures of performance. The mean-square residual error and Strehl ratio are sensitive to variations of the photon noise in the wavefront sensor and to variations in the sensor spacing and the actuator spacing. In

contrast, the resolution of the adaptive optics system, as measured by the PSF, shows little sensitivity to these variations. These performance metrics are very useful in the design of large-aperture telescopes using laser guide stars and slope sensors (12:1913).

Signal-to-Noise Ratio (SNR).

The single-frame SNR, as a function of spatial frequency, has been used to analyze the performance of two types of phase reconstructors: 1) the least-squares reconstructor and 2) the minimum variance reconstructor. The SNR adds to analysis of the mean OTF by including the effects of the variance of the OTF. This SNR metric demonstrates that the minimum-variance reconstructor performs better than the least-squares reconstructor for both the fully-compensated and partially-compensated scenarios (8:451) (7:4232).

AEOS Metrics.

On the basis of the analyses presented in the literature, the following metrics were chosen for characterization of AEOS performance:

- Pupil-Averaged Mean-Square-Residual Phase Error,
- Ensemble-Averaged Optical Transfer Function, and
- Signal-to-Noise Ratio.

These measures were chosen because they each provide complementary information on the character of the system. The mean-square-residual phase error characterizes the effectiveness of the deformable mirror correction by comparing the incoming phase to the phase applied by the mirror. The OTF quantifies the impact of these corrections upon the overall system transfer functions. This is useful since system resolution is directly related to the frequency attenuation experienced by incoming wavefronts. The SNR adds to the mean OTF a consideration of the fluctuations in the OTF. Together, these three metrics provide the necessary data needed to analyze overall system performance.

Summary of Key Results

The focus of this research is on the effects of actuator misalignment and actuator failure. It will be shown that the impacts of both are predictable and significantly less than intuition would predict. The impact of the misalignments and failures upon system performance will be shown to be dependent upon the seeing conditions:

- Object radiance at the WFS (ph),
- Fried atmospheric coherence parameter (r_0), and
- The effective movement of the wavefront across the pupil due to time delays between measurement and correction ($v\tau$).

Although performance varies depending upon seeing conditions, in all cases the performance degrades rather gracefully. Under most conditions, the system sustains only minimal degradation even for actuator misalignments of 20 percent of the actuator grid separation. For all seeing conditions, it was found that a misalignment of 5 percent of the actuator separation produced virtually identical results when compared to the perfect alignment case. For the case of failed actuators, the system does not appear to be affected until at least 10 percent of the actuators have failed and been removed. Again the degradation is graceful. As with the misalignment cases, the 5 percent failure cases were almost identical to the no-failure cases for all seeing conditions tested.

It was also determined that the SUN Sparc 2 workstations do not have the numerical accuracy to perform the numerical simulations for the AEOS 3.67-meter telescope. The 32-bit data accuracy of the Sparc 2s was insufficient to invert the 741 by 741 matrix necessary for calculation of the optimal reconstruction matrix. For this reason, the simulations were performed using the AMOS 1.6-meter telescope configuration. Further investigation using more advanced tools is recommended for specific characterization of the AEOS telescope.

Organization of Material

The remainder of this thesis is organized into four chapters. Chapter 2 describes the model and theory behind the simulation of an adaptive optics system. Descriptions of the numerical simulation and research procedure used are presented in Chapter 3. Chapter 4 presents the results of the simulations and an overall analysis of their importance to the design and operation of large-aperture adaptive-optic telescopes. Final conclusions are presented in Chapter 5. Additional information, including detailed parameters and results for each simulation, is included in the appendix.

II. THEORY AND MODELS

System Definitions and Assumptions

Consider a wavefront correction system (Figure 2-1) consisting of the telescope pupil, a deformable mirror (DM), a wavefront sensor (WFS), and a control law (12:1914).

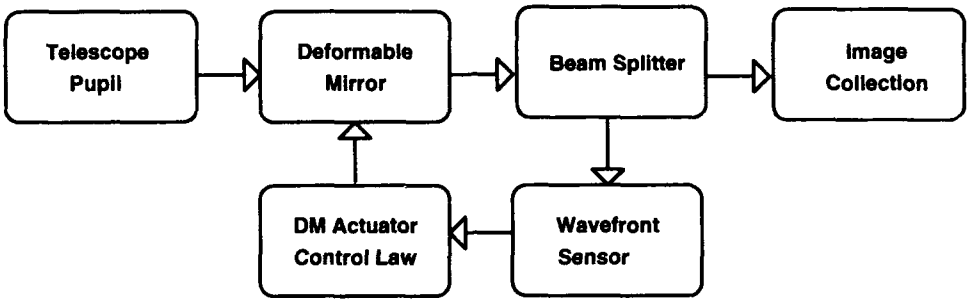

Figure 2-1 Block Diagram of Adaptive Optics System

The DM is located in a plane conjugate to the pupil plane of the telescope. A finite number of piezo-electric actuators control the surface figure of the mirror. The aperture is located in a plane conjugate to the WFS which divides the pupil into subapertures (Figure 2-2). The phase distortion in an incoming wavefront is determined by measuring the average wavefront slope within each subaperture. The control law converts these measurements into commands for the DM actuators. An inherent time delay, due to the process of calculation and application, exists for all AO systems. This delay means that the wavefront being corrected did not necessarily pass through the same turbulence as the measured wavefront. This additional source of error is expressed in terms of the distance the measured turbulence moves in the delay period.

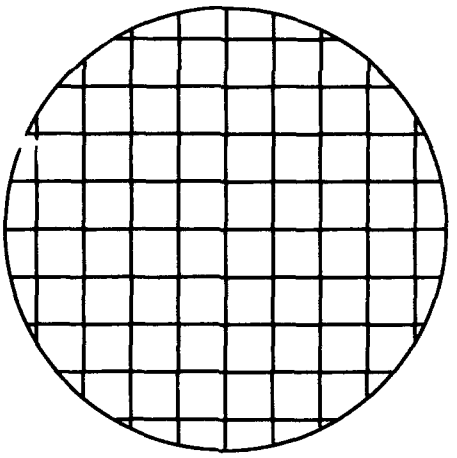

Figure 2-2 WFS Geometry Projected onto Pupil

An incoming wavefront is distorted by the turbulent atmosphere before reaching the pupil of the telescope. The phase correlation of the wavefront must be considered when modeling the distortion effects. Therefore, the distortion is modeled as a random phase screen in the pupil with spatial-phase structure function, D_ϕ, (10:7431)(12:1917-1919):

$$D_\phi(r) = 6.88\left(\frac{r}{r_0}\right)^{\frac{5}{3}} \tag{2-1}$$

where r_0 is the atmospheric coherence diameter and r is the magnitude of the separation of two points in the pupil of the telescope. A frozen, locally isotropic, random turbulence field moving at constant speed relative to the telescope is assumed. The turbulence is also assumed to be confined to the near field of the telescope and obey Kolmogorov statistics. The pupil of the telescope is described by the weighting function $W_A(x,y)$, where x and y are dimensions in the pupil plane. The function is normalized such that (12:1914):

$$\iint_{Pupil} W_A(x,y)dxdy = 1 \tag{2-2}$$

where the integral with respect to x and y is over the entire pupil plane. An incoming wavefront will have phase, $\psi(x,y,t)$, which is a random process realized at time, t. This phase is converted to a zero-mean phase, $\phi(x,y,t)$, by (12:1914):

$$\phi(x,y,t) = \psi(x,y,t) - \iint_{Pupil} W_A(x')\psi(x',t)dx'dy' \tag{2-3}$$

The WFS measures this incoming phase based upon the average slope of the incoming wavefront in each subaperture as shown in Figure 2-3 (12:1919). The telescope pupil is divided into square subapertures as projected from the WFS. The x and y direction slopes are measured in each subaperture. The displacement of the spot, in x and y, will determine the slope of the incoming wavefront and thus the phase.

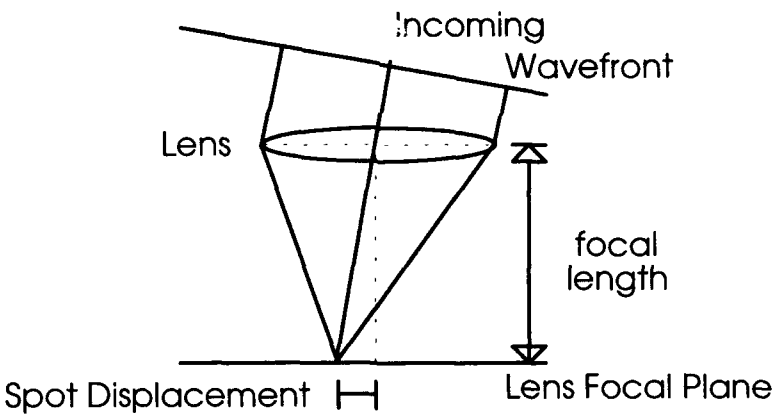

Figure 2-3 Single Subaperture Slope Measurement

The output of the n^{th} sensor as a noisy measurement of the average slope of $\phi(x,y,t)$ over a subaperture defined by $W_n(x,y)$ (12:1914):

$$s_n(t) = \iint_{Pupil} W_n(x,y)\left[\nabla\phi(x,y,t) \bullet \delta_n\right]dxdy + \alpha_n(t) \tag{2-4}$$

where

- $s_n(t)$ is the slope sensor output signal from the n^{th} sensor at time t (in rads/m),
- $W_n(x,y)$ is the weighting function for the n^{th} sensor (in m^{-2}) normalized so that:

$$\iint_{Subap} W_n(x,y)dxdy = 1 \tag{2-5}$$

- $\nabla\phi(x,y,t)$ is the spatial gradient of ϕ,
- δ_n is a unit vector in the direction of the sensitivity of the n^{th} sensor, and
- $\alpha_n(t)$ is the slope measurement error for the n^{th} sensor at time t (in rads/m).

The slope measurement error arises from noise in the detection process and is assumed to be independent of $\phi(x,y,t)$.

The control law generates a command for each actuator of the DM using a linear combination of the slope measurements from a Hartmann-type WFS. The actuator drive signal, $c_j(t)$, is defined (12:1914):

$$c_j(t) = \sum_{\forall n} M_{jn} s_n(t) \tag{2-6}$$

where $c_j(t)$ is the command sent to the j^{th} actuator and M_{jn} is the weighting of the n^{th} sensor signal in the j^{th} actuator command. M_{jn} is optimized by minimizing the mean-squared phase error produced by the compensation (7:4229). The influence functions are defined as spatial Gaussians given by (7:4229):

$$r_j(x,y) = exp\left(\frac{-\left(\left|x-x_j\right|^2 + \left|y-y_j\right|^2\right)}{L^2}\right) \tag{2-7}$$

where x_j is the center of the j^{th} actuator, and L is the 1/e width of the influence function.

The wavefront due to the mirror, $\phi_r(x,y,t)$, is (12:1915):

$$\phi_r(x,y,t) = \sum_{\forall j}\left[\int_{-\infty}^{t} c_j(\xi)\boldsymbol{r}_j(x,y,t-\xi)d\xi\right] \tag{2-8}$$

where $\boldsymbol{r}_j(x,y,\xi)$ is the impulse response of the DM at position x, and time ξ due to a unit impulse command to the j^{th} actuator at time, t. Assuming the response of the mirror is near instantaneous, the phase of the DM may be written as:

$$\phi_r(x,y,t) = \sum_{\forall j} c_j(t)\boldsymbol{r}_j(x,y) \tag{2-9}$$

When considering the control system delay effects, the convolution in Equation (2-8) must be evaluated (12:1915). Taylor's frozen-field hypothesis is used to analyze the effects of temporal delays (3:386). In Taylor's model, the spatial effects of short time delays are modeled by assuming that the incoming wavefront, to be corrected, is equivalent to the measured wavefront displaced by $v\tau$, where v is the turbulence velocity across the pupil and τ is the control delay time.

Performance Metrics

Mean-Square-Residual Phase Error.

The pupil-averaged mean-square-residual phase error, ε^2, gives a direct measure of the effectiveness of the correction applied by the deformable mirror. For the system we are considering, with a time delay of τ, the ε^2 in the pupil is (8:458):

$$\left\langle \varepsilon^2 \right\rangle = \iint_{Pupil} \boldsymbol{W_A}(x,y)\left\langle \varepsilon^2(x,y,\tau)\right\rangle dxdy \tag{2-10}.$$

where $\varepsilon(x,y,\tau)$ is the residual phase error in the generalized pupil function after each individual application of the DM correction in the image ensemble. It is given as (8:455):

$$\varepsilon(x,y,\tau) = \phi(x,y,\tau) - \phi_{\boldsymbol{r}}(x,y,\tau) \tag{2-11}$$

where $\phi(x,y,\tau)$ is the incoming phase as given in Equation (2-3) and $\phi_r(x,y,\tau)$ is the phase of the DM calculated as (8:455):

$$\phi_r(x,y,\tau,t) = \sum_{\forall j} c_j(t) r_j(x,y,\tau) \tag{2-12}$$

ε^2 is desired to be small, and expected to increase as the AO system configuration is degraded. This expectation is confirmed by the results in Chapter 4.

Optical Transfer Function.

Unlike the residual phase error, the optical transfer function (OTF) includes a consideration of the phase correlations between the individual points of the wavefront. The OTF clearly illustrates the response of the optical system in the spatial frequency domain. High spatial frequencies are of particular interest, since it is in this region that the magnitude of the OTF indicates the ultimate spatial resolution of the system (12:1914). One useful metric is the average OTF of an ensemble of the random image realizations. The ensemble-average OTF of a compensated imaging system is calculated as (8:455):

$$\langle H(\rho) \rangle = \frac{\left\langle \iint_{Pupil} W_A(x,y) W_A(x-\rho, y-\rho) e^{j[\varepsilon(x,y)-\varepsilon(x-\rho,y-\rho)]} dxdy \right\rangle}{N} \tag{2-13}$$

where the shift variable, ρ, is related to the spatial frequency vector, f, by (8:455):

$$f = \frac{\rho}{\lambda d_f} \tag{2-14}$$

where d_f is the focal length of the telescope and the normalizing quantity, N, is (8:455):

$$N = \iint_{Pupil} \left| \boldsymbol{W_A}(x,y) \right|^2 dxdy \tag{2-15}$$

$\langle \boldsymbol{H}(\rho) \rangle$ is desired to be as close as possible to diffraction limited performance. The results in Chapter 4 characterize this degradation.

Signal-to-Noise Ratio.

The signal-to-noise ratio (SNR) includes the effects of fluctuations in the OTF by considering the variance, as well as the mean OTF. The image spectrum SNR is (10:7430):

$$\boldsymbol{SNR}(u,v) = \frac{\left| E[\boldsymbol{D}(u,v)] \right|}{\left\{ var[\boldsymbol{D}(u,v)] \right\}^{1/2}} \tag{2-16}$$

where u and v are spatial frequencies, $\boldsymbol{D}(u,v)$ is the Fourier transform (spectrum) of the measured image, E is the expectation operator, and var is the variance operator. It has also been shown that the Short exposure SNR, $\boldsymbol{SNR_{se}}$ can be written (10:7430):

$$\boldsymbol{SNR_{se}}(u,v) = \frac{K \left| E_{se}[\boldsymbol{H}(u,v)] \boldsymbol{O}(u,v) \right|}{\left\{ K + K^2 \left| \boldsymbol{O}(u,v) \right|^2 var[\boldsymbol{H}(u,v)] \right\}^{1/2}} \tag{2-17}$$

where K is the average number of photo events per image, $\boldsymbol{O}(u,v)$ is the object spectrum normalized to unity at $(u,v) = (0,0)$, and $E_{se}[\boldsymbol{H}(u,v)]$ is the mean short-exposure compensated OTF of the system. Use of the short-exposure OTF denotes the OTF which would be measured with the atmospheric turbulence frozen in time. Long-exposure images will produce residual tilt errors in the wave, but these errors can be removed by recentroiding the images during post-processing.

It has been noted that a single frame SNR will be less than one at most spatial frequencies (7:4232). The single-frame SNR can be improved through averaging multiple realizations of an image, resulting in (10:7431):

$$SNR_N(u,v) = \sqrt{N}\left(SNR_{se}(u,v)\right) \tag{2-18}$$

where SNR_N denotes the SNR resulting from the averaging of N images. The higher the SNR of the system for a given spatial frequency, the more likely that frequency can be reconstructed in the final image. Since the resolution of the the final image is directly proportional to the fraction of the original frequencies which can be reconstructed, the SNR is desired to remain high at all frequencies and expected to drop off at all frequencies as the AO system is degraded. The results in Chapter Four characterize this drop off in SNR similar to the OTF characterization.

III. SIMULATION AND APPROACH

Background

The approach taken is based largely upon models and analyses described in the literature review. The adaptive optics simulation previously developed and used for adaptive optics performance analyses is the baseline for the research (8:459)(9:2000). The speed of the simulation compared to numerical integrations of theoretical expressions allowed us to accomplish significant characterizations within the research timeline. In order to achieve the research objectives, the code was modified to allow for modeling :

- The 3.67-meter AEOS telescope system,
- The 1.6-meter AMOS telescope system,
- The effects of misalignment between the pupil and the DM, and
- The effects of failed actuators.

Once these embellishments were complete, runs were made to verify their accuracy. In the process, it was determined that the Sun Sparc 2 computer systems did not have the numerical accuracy to perform the simulations for the 3.67-meter case. The 32-bit data accuracy of the Sparc 2s was insufficient to invert the 741 by 741 matrix necessary for calculation of the optimal reconstruction matrix. After extensive attempts at work-arounds, the analyses were performed using the current 1.6-meter AMOS telescope system as a baseline.

Adaptive Optics Simulation

The usefulness of numerical simulation versus analytic calculations has been previously demonstrated (8:459). Theoretical calculations of the average OTF are very time consuming, requiring accurate evaluation of a two-dimensional numerical integration at every point the average OTF is computed. Calculating the second moment of the OTF is even more difficult, as a four-dimensional integration is required. Also, for the tilt-

removed case, simulations will provide more accurate results than theoretical calculations (8:459). For these reasons, the numerical simulation described below was used to generate the results analyzed in Chapter Four.

The adaptive optics simulation consists of three parts:

- Setup of the telescope pupil and simulation parameters,
- Iterations of the atmospheric distortion, measurement, correction, and accumulation of statistical quantities, and
- Computations of statistics and data output.

The first part sets up:

- Templates for the telescope pupil and wavefront subapertures,
- The optimal positions of the deformable mirror actuators,
- Modifications to actuator locations to simulate misalignment or failure,
- The optimal wavefront reconstruction matrix, and
- The random phase screen generator.

The main iteration process calculates:

- A realization of a random turbulence induced phase screen in the telescope pupil
- Wavefront sensor measurements,
- Actuator commands,
- Time delay effects (if selected by user),
- Effect of the actuators' response upon a future wavefront,
- The residual phase error after compensation, and
- The instantaneous single-frame optical transfer function (OTF).

The final part of the simulation:

- Accumulates and averages the single-frame OTFs,
- Calculates the mean and variance for the overall pupil OTF,
- Outputs the data into files for further data analysis, and

- Calculates the mean-square-residual phase error across the pupil.

Figure 3-1 shows the functional block diagram of the simulation.

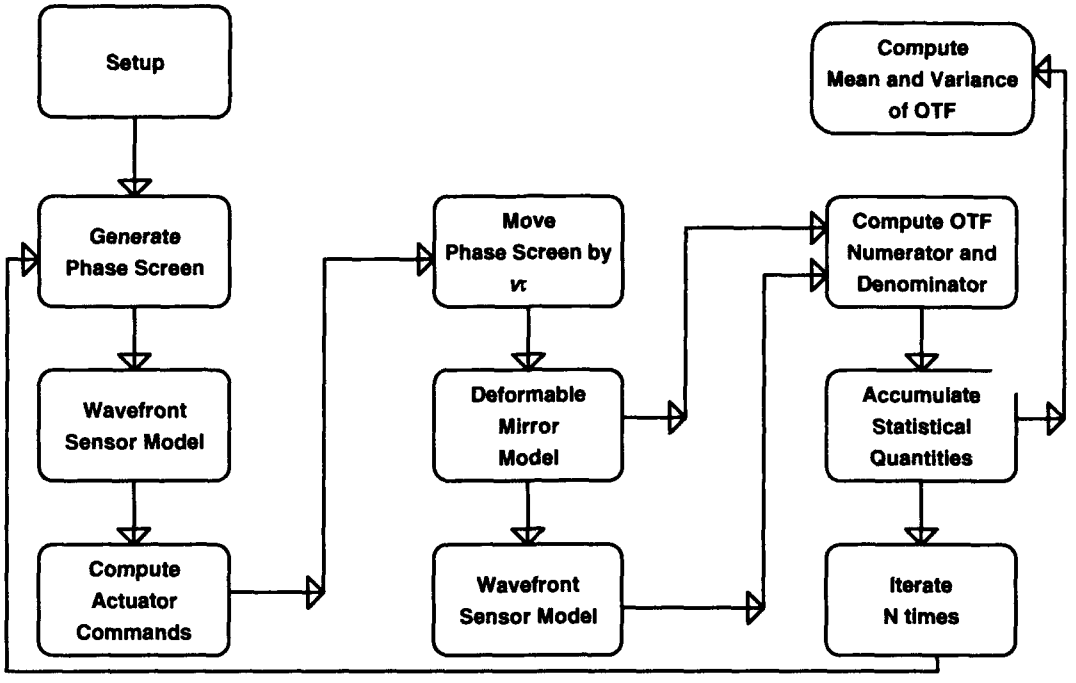

Figure 3-1 Block Diagram of Adaptive Optics Simulation (8:460)

The Setup block sets up the telescope pupil and performs all of the one-time calculations necessary for the rest of the simulation. In addition to the telescope pupil template, the wavefront sensor (WFS) subaperture and deformable mirror (DM) actuator locations are calculated. The optimal least-squares reconstruction matrix, M_{jn}^{LS}, is computed using a routine which minimizes the difference between the WFS measured slopes, s_n, and those caused by a set of actuator commands, c_j. Although it has been shown that minimizing the pupil-averaged mean-square phase error using the optimal minimum-variance reconstruction matrix, M_{jn}^{MV}, gives slightly better performance than the least-squares method, the M_{jn}^{LS} matrix is significantly more computationally efficient and is therefore employed for this research (8:457). The M_{jn}^{LS} matrix is computed for the case of Gaussian actuator influence functions.

Once the setup calculations are complete, the main iteration loop is begun. The first step is to simulate the atmospheric turbulence effects. This is simulated as a random phase screen in the pupil of the telescope. The technique for computing these realizations of a random phase screen is from Cochran (8:460). This method is known to produce phase screens which exhibit a structure function, when computed over large ensembles of phase screens, equal to the theoretical expression for the structure function based upon Kolmogorov statistics (8:454,460).

For each iteration, after the atmospheric turbulence is applied, wavefront sensor (WFS) measurements are computed (8:454) with WFS noise simulated in each measurement by adding a realization of a zero-mean Gaussian random variable with standard deviation of, σ_n. σ_n is given by (9:2000):

$$\sigma_n = \begin{cases} \dfrac{0.86\pi\eta}{SNR_v r_0} & L > r_0 \\ \dfrac{0.74\pi\eta}{SNR_v L} & L \le r_0 \end{cases} \tag{3-1}$$

where r_0 is the atmospheric diameter, L is the length of one side of a subaperture, η is an efficiency factor, and SNR_v is the voltage SNR in the WFS plane, given by (9:2001):

$$SNR_v = \frac{K_w}{\sqrt{K_w + Q_w \sigma_{rms}}} \tag{3-2}$$

where K_w is the average number of photons per integration time in each subaperture (same as ph), Q_w is the number of pixels in the subaperture detector plane, and σ_{rms} is the rms number of read noise electrons per pixel per integration time in the subaperture detector. This noise variance, σ_n^2, is affected by the average number of photo-events per subaperture per integration time. In the simulation, this value is selectable by the user since in real operations the brightness of the target object will determine the number of

photons available to drive the WFS. Brighter objects will produce better measurements since the WFS SNR will be higher due to the larger incoming signal.

The WFS measurements are used to calculate the appropriate actuator commands, c_j, using the reconstruction matrix, M_{jn}^{LS}. At this point, the phase of the DM, $\phi_r(x,y)$, is calculated and subtracted from the incident phase at the pupil, $\phi(x,y)$. This operation produces a map of the residual phase error, $\varepsilon(x,y)$, in the pupil of the telescope. This residual error is a measure of the effectiveness of the DM compensation. Quantities are accumulated from the $\varepsilon(x,y)$ arrays and used to calculate the overall mean-square-residual phase error across the pupil.

For each image, the residual phase in the pupil is used to compute a single realization of the OTF of the system using standard Fourier methods (8:460). The complex-valued OTF and the real-valued squared modulus of the OTF are accumulated for each OTF realization. Once the appropriate number of frames have been simulated, the arrays containing the accumulated mean and variance of the OTF at every spatial frequency are stored. These arrays are also used to calculate the image spectrum SNR of the system.

Simulation Modifications

For both the shifted actuator and the failed actuator cases, the code modifications were made as part of the setup of the simulation. The simulated misalignments are applied after the reconstruction matrix is generated based upon the original actuator locations. The simulated failed actuators are removed from the DM before the reconstruction matrix is generated. In both cases, once the modified code is applied, the rest of the simulation continues according to the baseline.

To simulate the impact of a misalignment between the DM and the pupil, the user inputs the actuator shifts as a percentage of the actuator grid separation (*actsep*). Based upon the percent shift (*actshift*) chosen, a subroutine relocates the actuators as:

$$x_{shift} = (actsep) \times (actshift) \tag{3-3}$$

$$y_{shift} = (actsep) \times (actshift) \tag{3-4}$$

$$x_{new} = x_{old} + x_{shift} \tag{3-5}$$

$$y_{new} = y_{old} + y_{shift} \tag{3-6}$$

Since the shift is applied as both a horizontal shift and a vertical shift simultaneously, the actuators are misplaced by

$$shift_{diag} = (\sqrt{2}) \times (x_{shift}) \tag{3-7}$$

diagonally. Since this is an open-loop system, there is no feedback to the reconstruction command generator, so the reconstruction matrix will still generate DM commands based upon the original actuator locations.

The second modification made to the code was the addition of a routine to simulate the case of failed actuators. The failed actuators are chosen using a random draw without replacement from a population consisting of all the actuators. Although the failed actuators differ for different runs, the configurations are constant for the frames within a run. Although one can envision configurations which would perform differently, we only considered cases where the failed actuators were randomly and uniformly distributed throughout the pupil. In the end, the exact differences between runs were not statistically important, but rather, the overall trend and rate of change in the OTF and SNR produced by increasing the percentage of failed actuators.

There are three possible scenarios for modeling telescope performance with failed actuators:

1. Failed actuators are not removed, but reconstruction matrix is recalculated.
2. Failed actuators are drilled out and reconstruction matrix recalculated.
3. Failed actuators are failed without any recalculation.

To model scenario 1, the actuator influence functions of the failed actuators are set to zero as part of the routine which computes the optimal reconstruction matrix. This models the fact that the failed actuators would be frozen in place and would not allow the DM to deform at that point. Unfortunately, this implementation causes the reconstruction matrix to be rank deficient since it leaves columns of zeroes in the matrix. Additional analysis would be required to effectively model this situation.

Scenario 2 is modeled by simply removing the failed actuators from the array containing actuator locations. The optimal reconstruction matrix is calculated using the remaining actuators. The result is a configuration similar to that of limited-degree-of-freedom configurations (7:4230). Like those reduced-actuator cases, the system will have varying degrees of partial compensation, with 0 percent failure corresponding to full compensation (assuming the actuators are initially placed on a grid with spacing approximating the effective seeing diameter ($actsep = r_0$)) . This second case was chosen for our research since it most closely resembles the operational procedure followed by the AMOS operators. When determined necessary, the DM is removed; the failed actuators are drilled out; and the now partially-compensated DM is reinstalled.

Scenario 3 models the effect of failed actuators without removal. The effects are modeled by setting the actuator command for the failed actuators to zero. This avoids the problem of recalculating the reconstruction matrix and models the situation where the operators do not know the actuators are failed or choose not to compensate for them.

Procedure

Once the code was modified to simulate the misalignments and failed actuators, runs were performed to verify the coding changes. The new code was run with both 0 percent shift as well as 0 percent failure configurations. The results were identical to the baseline code. With the code verified, a series of runs were performed which characterize the performance degradation with respect to increasing misalignments or additional actuator

failure. Tables A-1 and A-2 in the appendix, list the important seeing conditions of each configuration run for both the misaligned actuator and failed actuator cases. Throughout the runs, the baseline configuration was similar to the existing Air Force Maui Optical Site (AMOS) 1.6-meter telescope (10:7429).

The baseline configuration parameters for the AMOS simulations are shown in Table 3-1. The variable seeing parameters are shown in Table 3-2 along with the misalignment and failure parameters. These parameters were varied as shown in Table 3-3; specifics for each run are given in Tables A-1 and A-2. The resulting OTF and SNR were plotted with r_0, *ph*, and *vt* (each defined in Table 3-2) held constant showing the effects of 0, 5, 10, 20, 50 percent misalignment. The effects of failed actuators are shown for 0, 5, 10, 20, 50, 75 percent failed cases.

It is important to consider how the seeing conditions affect the overall performance. Thus, it was necessary to demonstrate how seeing conditions affected the performance impact of the misalignments and failures. To this end, the varying misalignment and failure cases were run for a variety of operational conditions defined by the seeing parameters (r_0, *ph*, *vt*) as listed in Table 3-3:

Table 3-1 Constant Baseline Parameters for Simulation

100	=	number of image frames averaged
16	=	number of subapertures across the pupil diameter
1.6	=	diameter of primary mirror (meters)
0.335	=	diameter of secondary mirror (meters)
0.5e-6	=	imaging wavelength (meters)
0.5e-6	=	WFS wavelength (meters)
1	=	adaptive optics correction applied (1 = yes)
1	=	tilt correction applied (1 = yes)
0.11	=	actuator grid separation (meters)

Table 3-2 Variable Parameters

r_0	=	Fried seeing parameter (effective telescope diameter w/o AO)
ph	=	avg # of photo-events per subaperture per integration time for WFS
vt	=	turbulence movement due to system time delay (meters)
sh	=	DM misalignment (% of actuator separation)
x	=	percent of actuators failed

Table 3-3 Variation of Parameters for Simulation Runs

r_0	$\Rightarrow$	07	10	13	(cm)
ph	$\Rightarrow$	2.0e6	100	25	(photo/subap/frame)
vt	$\Rightarrow$	00	05	10	(cm)

Tables A-1 and A-2 show the parameters for every run. The r_0 values considered are typical of the possible conditions at AMOS. The ph values correspond to WFS SNR values of : infinity, 10, and 5, respectively. The vt values correspond to typical wind

speeds and WFS integration times for AMOS. These variations have been previously used to characterize OTF and SNR performance across the realm of realistic seeing conditions (9:2001). The results are presented and analyzed in Chapter Four.

Performance Metrics

In order to characterize the performance of the system, we use the following three metrics:

- Radial averaged OTF,
- Radial averaged SNR, and
- Mean-square-residual phase error

to analyze performance. Each has been used in the literature (9:2001)(12:1915).

As part of the simulation, the complex-valued mean and variance of the OTF are stored in output arrays. By averaging the array elements which correspond to the same radial distance from the optical axis of the telescope pupil, the average OTF, as a function of radial position in the pupil, is calculated. The output is plotted versus spatial frequency normalized to the size of the pupil used. The OTF is used to characterize the system throughput of the misaligned and failed actuator configurations.

SNR results characterize the quality of the OTF for the various runs (9:1999). The pointwise SNR was calculated by taking the real-valued modulus of the mean OTF and dividing by the square root of the real-valued modulus of the variance at every point in the pupil. The calculations assume the imaging of an unresolvable star producing mean number of photo-events per integration time, K_W (or ph), for each subaperture. The result is then radially averaged to get the unnormalized radially averaged SNR. Similar to the OTF, the SNR is plotted versus spatial frequency normalized to the pupil.

Another metric calculated by the simulation is the mean-square-residual phase error, ε^2, described in detail in the literature (12:1915) (11:1771). The ε^2 is an excellent metric for obtaining the optimal reconstruction matrix (minimum-variance), as well as a

measure of the effectiveness of the actual conjugate phases applied by the DM. The simulation calculates ε^2 by accumulating the residual phase errors from each frame, at the end of each iteration, and then compiles the average over all frames. As the effectiveness of the compensation degrades due to misalignments or failures, ε^2 will increase consistently. This metric is used to analyze the effectiveness of the misaligned actuators.

IV. RESULTS

Actuator Misalignment

The results of the misapplication of actuator commands due to the actuator misalignments are now presented. As previously stated, the pupil-averaged mean-square-residual phase error, ε^2, the average optical transfer function (OTF), and the system signal-to-noise ratio (SNR) are used to characterize the overall system performance. In order to better quantify the relative effects of each misalignment case relative to the perfect alignment baseline, the percentage change in performance is presented for each metric used. The percentage change is calculated as:

$$Percent\ Change = 100 \times \frac{\left| PM_0 - PM_n \right|}{PM_0} \tag{4-1}$$

where PM_0 is the baseline value of the performance metric, and PM_n is the misaligned value of the performance metric.

Mean-Square-Residual Phase Error.

The effects of deformable mirror misalignment on the wavefront correction as measured by ε^2 are quantified in Table 4-1, Table 4-2, and Table 4-3. As expected, the error increases consistently with increased misalignment. The effect is most pronounced for the worst seeing conditions. The system is less vulnerable to the misalignment induced error when the object is bright (high ph) or the atmospheric turbulence is calm (high r_0).

Table 4-1 ε^2 for Actuator Misalignment (r_0 = 7 cm)

Misaligned Actuators						
r0 (cm)	*ph* (ph/sa)	$v\tau$ (cm)	*Shift* (%)	ε^2	Change	Total Change
7	2000000	0	0	8.38699		
7	2000000	0	5	8.41394	0.32%	0.02695
7	2000000	0	10	8.50522	1.41%	0.11823
7	2000000	0	20	8.89033	6.00%	0.50334
7	2000000	0	50	12.2141	45.63%	3.82711
7	100	0	0	8.58295		
7	100	0	5	8.6105	0.32%	0.02755
7	100	0	10	8.70535	1.43%	0.1224
7	100	0	20	9.11156	6.16%	0.52861
7	100	0	50	12.8662	49.90%	4.28325
7	25	0	0	9.58563		
7	25	0	5	9.61921	0.35%	0.03358
7	25	0	10	9.73241	1.53%	0.14678
7	25	0	20	10.22897	6.71%	0.64334
7	25	0	50	15.5252	61.96%	5.93957

Table 4-2 ε^2 for Actuator Misalignment (r_0 = 10 cm)

Misaligned Actuators						
r0 (cm)	*ph* (ph/sa)	$v\tau$ (cm)	*Shift* (%)	ε^2	Change	Total Change
10	2000000	0	0	4.62861		
10	2000000	0	5	4.64349	0.32%	0.01488
10	2000000	0	10	4.69386	1.41%	0.06525
10	2000000	0	20	4.90638	6.00%	0.27777
10	2000000	0	50	6.74077	45.63%	2.11216
10	100	0	0	4.68208		
10	100	0	5	4.69699	0.32%	0.01491
10	100	0	10	4.74834	1.42%	0.06626
10	100	0	20	4.96737	6.09%	0.28529
10	100	0	50	6.9475	48.38%	2.26542
10	25	0	0	5.0281		
10	25	0	5	5.04502	0.34%	0.01692
10	25	0	10	5.10271	1.48%	0.07461
10	25	0	20	5.35337	6.47%	0.32527
10	25	0	50	7.88211	56.76%	2.85401

Table 4-3 ε^2 for Actuator Misalignment (r_0 = 13 cm)

Misaligned Actuators						
r0 (cm)	*ph* (ph/sa)	$v\tau$ (cm)	*Shift* (%)	ε^2	Change	Total Change
13	2000000	0	0	2.98903		
13	2000000	0	5	2.99864	0.32%	0.00961
13	2000000	0	10	3.03117	1.41%	0.04214
13	2000000	0	20	3.16841	6.00%	0.17938
13	2000000	0	50	4.35299	45.63%	1.36396
13	100	0	0	3.06079		
13	100	0	5	3.07062	0.32%	0.00983
13	100	0	10	3.10446	1.43%	0.04367
13	100	0	20	3.2494	6.16%	0.18861
13	100	0	50	4.59069	49.98%	1.5299
13	25	0	0	3.42523		
13	25	0	5	3.43727	0.35%	0.01204
13	25	0	10	3.47777	1.53%	0.05254
13	25	0	20	3.65554	6.72%	0.23031
13	25	0	50	5.55652	62.22%	2.13129

The percentage change in residual error is only slightly dependent upon the object brightness. Comparison of the 25, 100, and the 2,000,000 photons per subaperture cases, indicates that the percentage change, as well as the total change, in error increase consistently as the misalignment increases. Brighter objects will produce lower total error and, thus, better AO corrections due to the higher WFS SNR produced by a greater number of incoming photons. The higher SNR allows better phase measurements and results in more accurate correction commands. Since the commands are more accurate to begin with, the effect of a specific percentage increase in error will have less overall effect on the applied correction.

The effect of the Fried parameter is similar to that of object brightness. The percentage changes in ε^2 for the $r0$ = 7 cm cases (Table 4-1) are identical to the changes for the $r0$ = 10 cm and 13 cm cases (Tables 4-2 and 4-3). While the percentage change in error is virtually independent of the atmospheric conditions, the total change in error is much more for low values of the Fried parameter. Since the incoming wavefront will require less correction when r_0 is large than when it is small, the necessary actuator commands will be smaller in magnitude. Therefore, the misapplication of these commands (due to misalignment) will have a less detrimental effect, and the resulting residual error will be lower.

The effects of the misalignments as related to system time delays ($v\tau$), are shown in Table 4-4 and Table 4-5. They indicate that the misalignments will affect these systems in much the same way as the systems with instantaneous correction. The percentage change in residual error is still only slightly dependent upon the object brightness. Comparison of the 25, 100, and the 2,000,000 photons per subaperture cases indicates that the percentage change, as well as the total change, in error increase consistently as the misalignment increases.

The effect of the time delay is similar to that of the Fried parameter. The percentage changes in ε^2 for the $v\tau$ = 5 cm cases are almost identical to the changes for the $v\tau$ = 10 cm cases. While the percentage change in error is virtually independent of the time delay, the total change in error is much more for high values of the $v\tau$. Since the measured wavefront will more closely approximate the wavefront being corrected when $v\tau$ is small than when it is large, the necessary actuator commands will be more appropriate. Therefore, the misapplication of these commands (due to misalignment) will have a less detrimental effect and the resulting residual error will be lower.

Table 4-4 ε^2 for Actuator Misalignment with Time Delay (r_0 = 10 cm, $ph = 2\times10^6$)

Misaligned Actuators (with time delays)						
r0 (cm)	*ph* (ph/sa)	$v\tau$ (cm)	*Shift* (%)	ε^2	Change	Total Change
10	2000000	5	0	21.2791		
10	2000000	5	5	21.4096	0.61%	0.1305
10	2000000	5	10	21.5703	1.37%	0.2912
10	2000000	5	20	21.9842	3.31%	0.7051
10	2000000	5	50	24.2875	14.14%	3.0084
10	2000000	10	0	30.3735		
10	2000000	10	5	30.5531	0.59%	0.1796
10	2000000	10	10	30.7515	1.24%	0.378
10	2000000	10	20	31.207	2.74%	0.8335
10	2000000	10	50	33.4178	10.02%	3.0443

Table 4-5 ε^2 for Actuator Misalignment with Time Delay (r_0 = 10 cm, ph = 25)

Misaligned Actuators (with time delays)						
r0 (cm)	*ph* (ph/sa)	$v\tau$ (cm)	*Shift* (%)	ε^2	Change	Total Change
10	25	5	0	21.6495		
10	25	5	5	21.7875	0.64%	0.138
10	25	5	10	21.9676	1.47%	0.3181
10	25	5	20	22.4701	3.79%	0.8206
10	25	5	50	26.1303	20.70%	4.4808
10	25	10	0	30.8215		
10	25	10	5	31.0109	0.61%	0.1894
10	25	10	10	31.2306	1.33%	0.4091
10	25	10	20	31.7783	3.10%	0.9568
10	25	10	50	35.3504	14.69%	4.5289

The overall implication of the mean-square-residual phase error results is that the effects of DM misalignments will be worse for dim objects, bad atmospheric conditions, and slow system response times. To further explore the effect of the decreased effectiveness of the AO compensation, the radially-averaged OTF is now investigated for the same cases.

Optical Transfer Function.

While the mean-square-residual phase error is a good measure of how well the system is applying corrections, the OTF provides a measure of overall system performance as a result of those corrections. The following figures show the radially-averaged OTFs plotted on a log scale. Additionally, plots of the percentage change in the OTF relative to the perfect alignment cases are shown to better quantify the effects relative to the baseline. It is clear that the effects of the misalignment are gradual since performance degrades gracefully. Although, the 5 percent misalignment case is within 5 percent of the baseline OTF for all seeing conditions, the capability of the system to absorb the impact of greater misalignment appears to be significantly better for the best seeing conditions. This is consistent with the ε^2 analysis.

Comparison of the 7-cm, 10-cm, and 13-cm Fried parameter cases in Figures 4-2, 4-4, and 4-6, shows that the percentage loss of information significantly increases as the atmospheric conditions degrade. At the relatively good seeing condition of r_0 = 13 cm, both the 5 percent and 10 percent misalignments are within 5 percent of the baseline OTF. Increasing turbulence to r_0 = 10 cm, increases the loss to 10 percent. With conditions at r_0 = 7 cm, the loss of information increases to 15 percent of the baseline. This dependence upon the Fried parameter results from the fact that the scale size of the fluctuations changes with r_0. Therefore, although misalignment errors impact small corrections by the same percentage in residual phase error as shown earlier, the performance impact will be greater when large corrections are applied.

Additionally, as the misalignment approaches the Fried parameter value, the performance degrades rapidly. For the r_0 = 7 cm, the 50 percent curve has a much lower cut-off frequency, about 0.35, than the other curves, about 0.9. At r_0 = 13 cm, the cut-off frequency for the 50 % curve is almost 0.95, almost identical to the other curves. This difference in cut-off frequencies is due to the relationship between the Fried parameter

and the actuator separation. At r_0 = 7 cm, the 50 percent misalignment case corresponds to 80 percent of the r_0 value, while at r_0 = 13 cm, the 50 percent misalignment case corresponds to only 40 percent of the r_0 value. As the misalignment approaches the Fried parameter, the AO compensation becomes ineffective.

The almost identical results of the 25 and the 2,000,000 photons per subaperture cases, for all r_0 values, indicate that the misalignment effects are independent of object brightness. For this reason, all other configurations were run only for the *ph* = 25 and *ph* = 2,000,000 cases. The major effect of object brightness on the AO system is the WFS SNR and thus the WFS measurement accuracy.

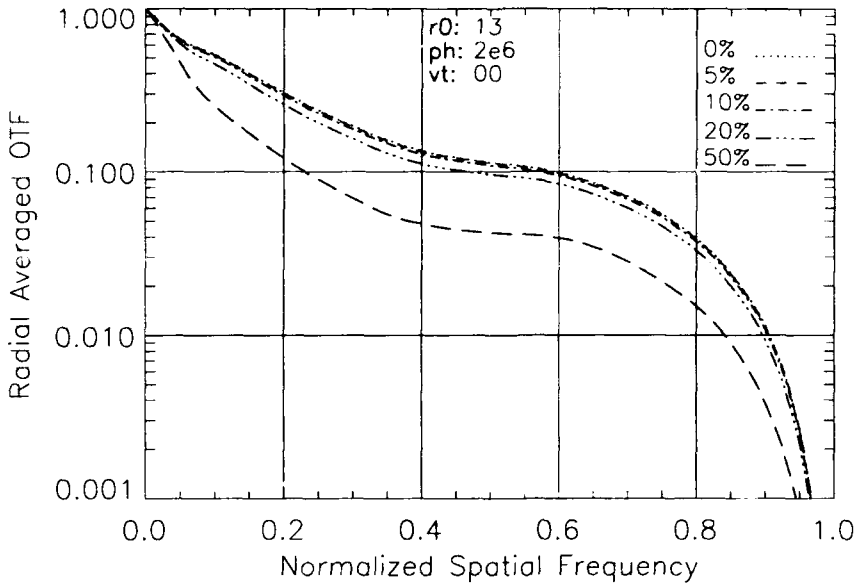

Figure 4-1 Misalignment Effects on Radial-Averaged OTF ($r_0 = 13$, $ph = 2\times10^6$, $v\tau = 0$)

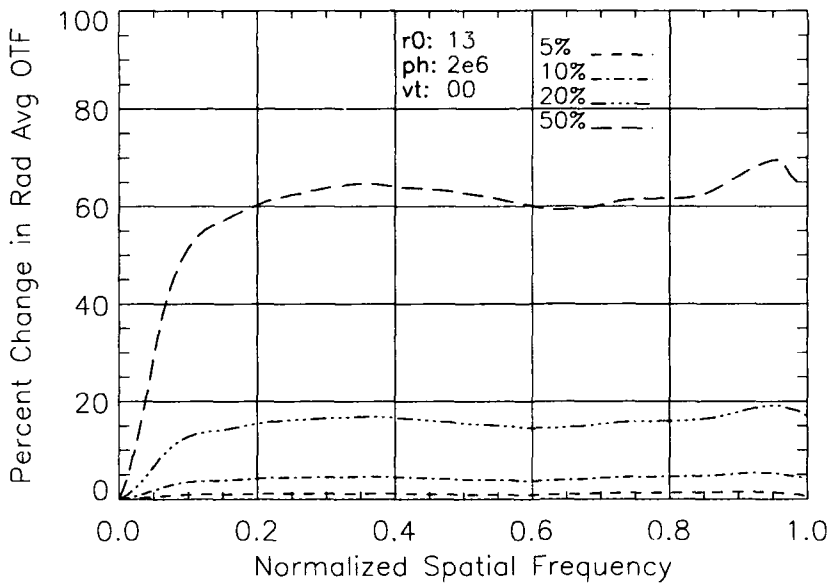

Figure 4-2 Misalignment Effects on Change in OTF ($r_0 = 13$, $ph = 2\times10^6$, $v\tau = 0$)

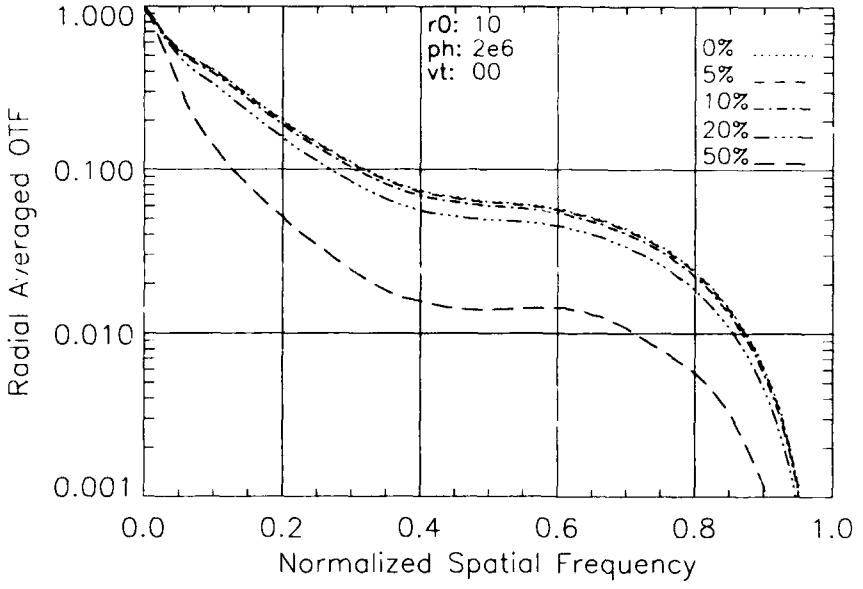

Figure 4-3 Misalignment Effects on Radial-Averaged OTF ($r_0 = 10$, $ph = 2\times10^6$, $v\tau = 0$)

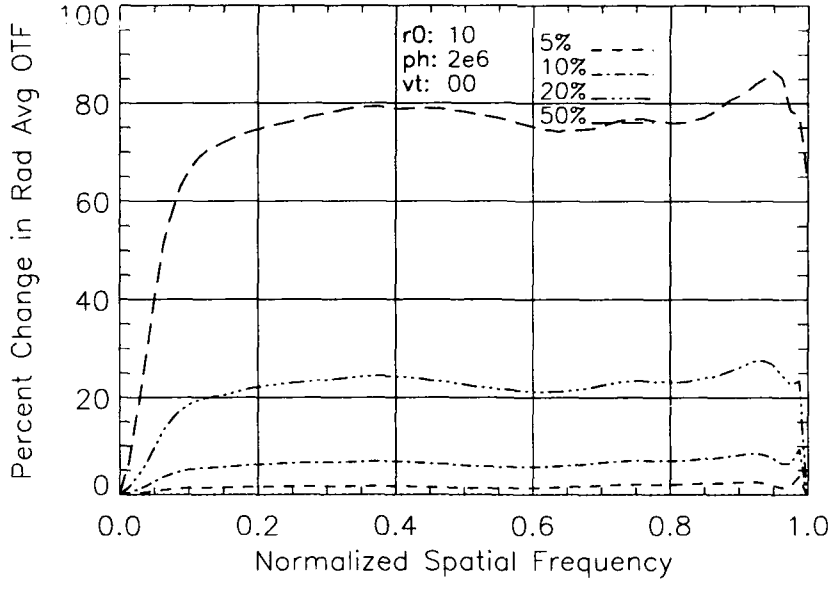

Figure 4-4 Misalignment Effects on Change in OTF ($r_0 = 10$, $ph = 2\times10^6$, $v\tau = 0$)

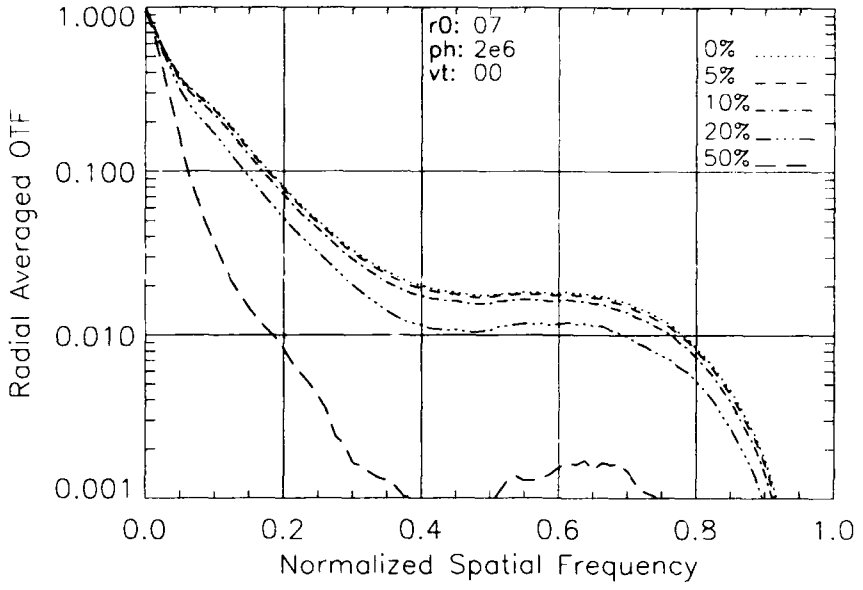

Figure 4-5 Misalignment Effects on Radial-Averaged OTF ($r_0 = 07$, $ph = 2\times10^6$, $v\tau = 0$)

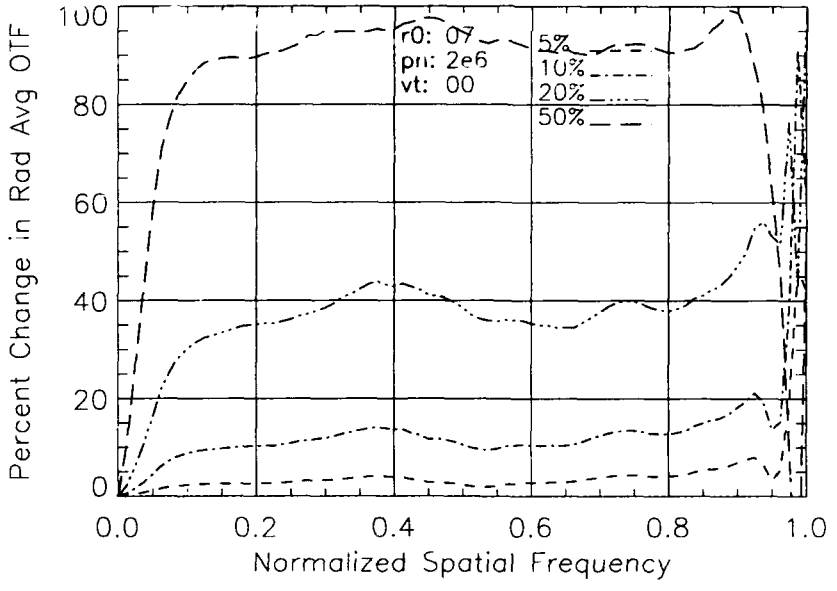

Figure 4-6 Misalignment Effects on Change in OTF ($r_0 = 07$, $ph = 2\times10^6$, $v\tau = 0$)

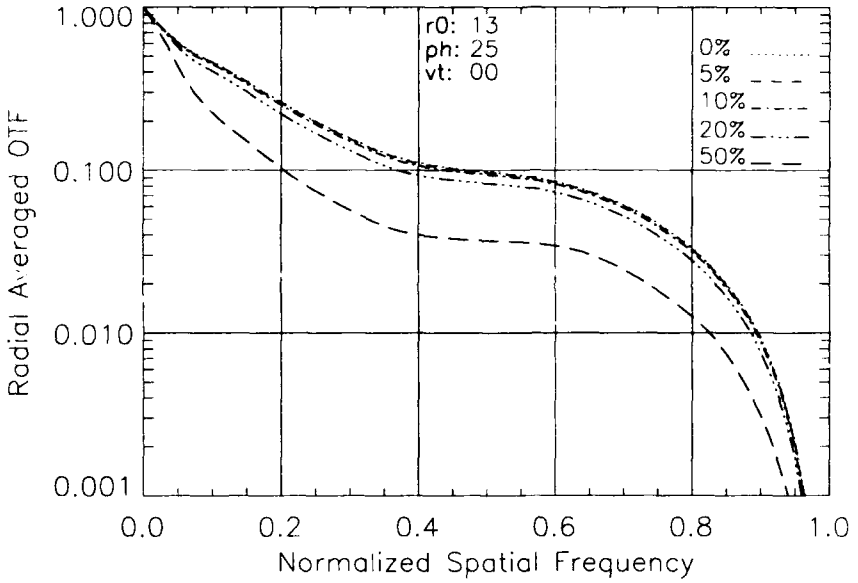

Figure 4-7 Misalignment Effects on Radial-Averaged OTF ($r_0 = 13$, $ph = 25$, $v\tau = 0$)

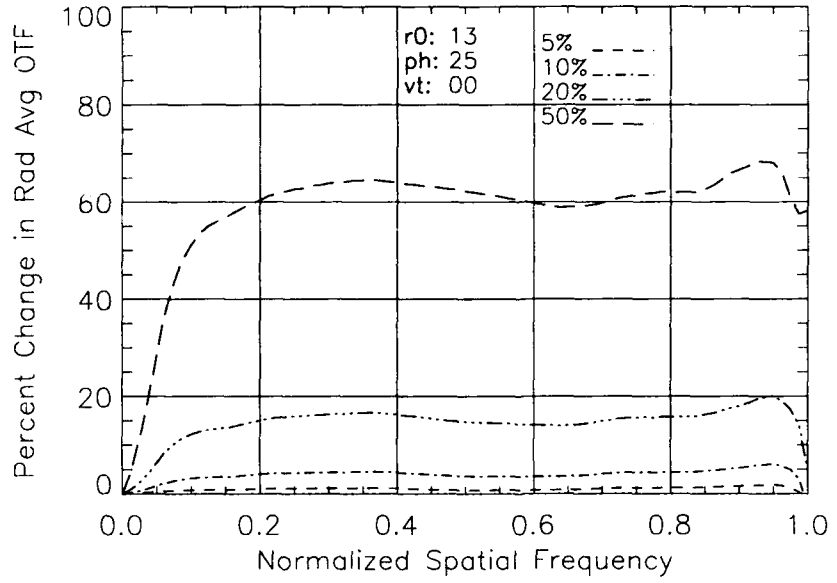

Figure 4-8 Misalignment Effects on Change in OTF ($r_0 = 13$, $ph = 25$, $v\tau = 0$)

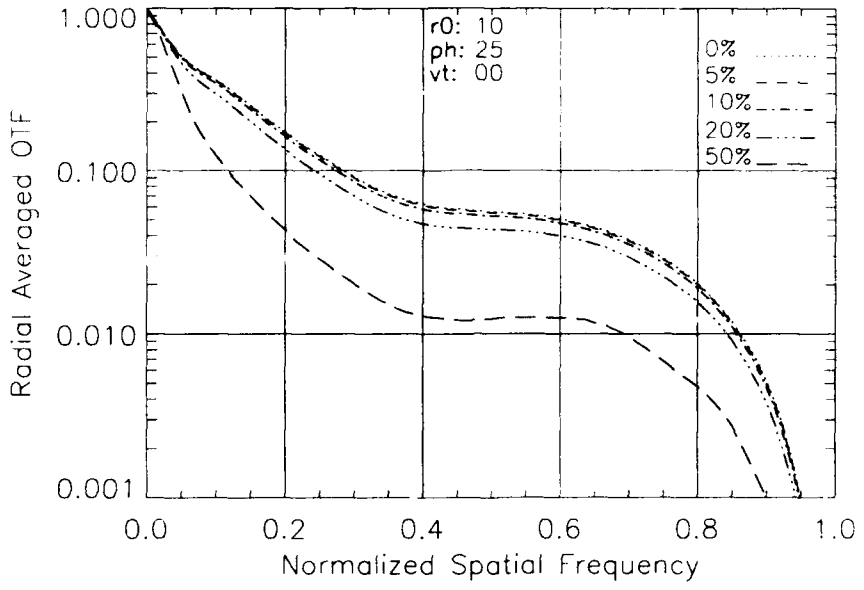

Figure 4-9 Misalignment Effects on Radial-Averaged OTF ($r_0 = 10$, $ph = 25$, $v\tau = 0$)

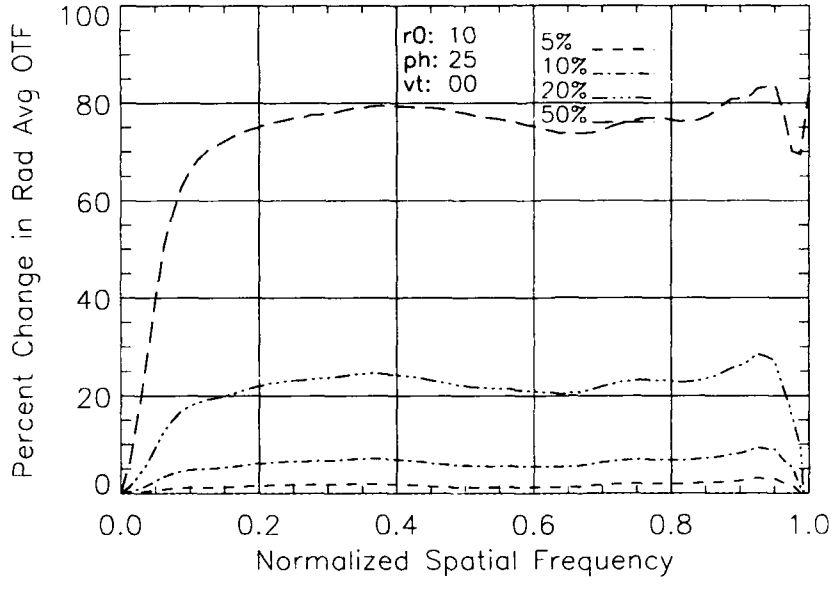

Figure 4-10 Misalignment Effects on Change in OTF ($r_0 = 10$, $ph = 25$, $v\tau = 0$)

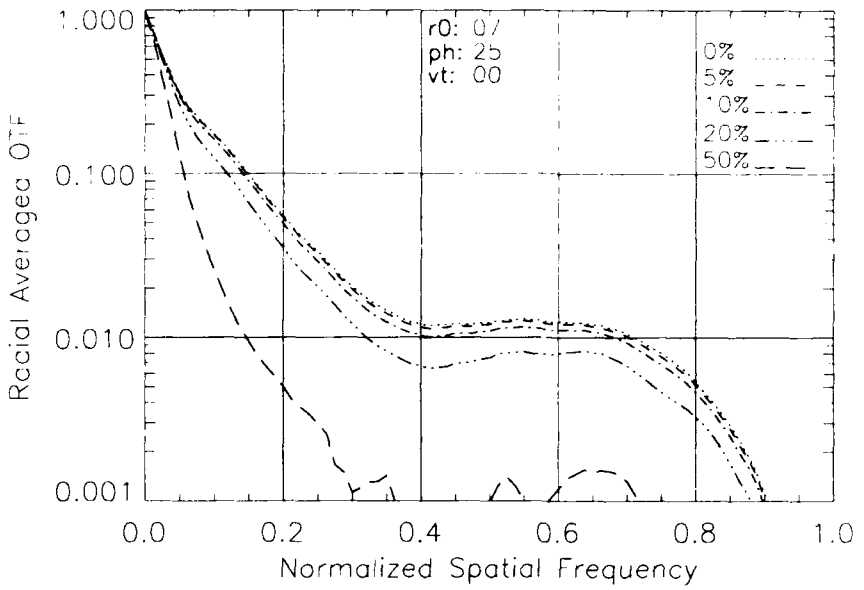

Figure 4-11 Misalignment Effects on Radial-Averaged OTF ($r_0 = 07$, $ph = 25$, $v\tau = 0$)

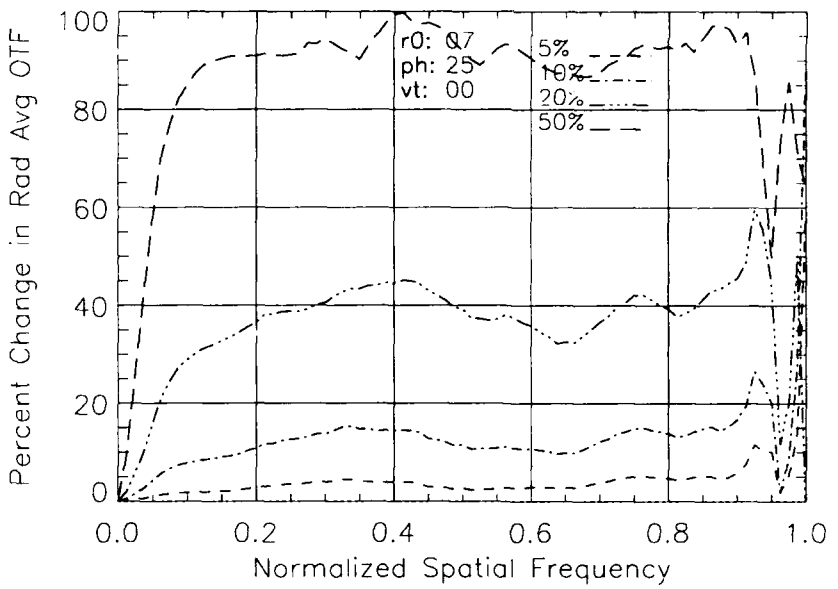

Figure 4-12 Misalignment Effects on Change in OTF ($r_0 = 07$, $ph = 25$, $v\tau = 0$)

The effects of the misalignments on OTF as related to system time delays ($\nu\tau$), are shown in Figures 4-13 and 4-14. They indicate that the misalignments will affect these systems in much the same way as the systems with instantaneous correction. As before, there is an independence of the object brightness. The increased separation of the OTF lines for the varied misalignments indicates a dependence upon the time delay experienced. Although the effects appear to be most severe for the poorest response time, the percentage loss in information does not change much for increased delay times. The misalignments still impact the overall performance gradually and predictably. Additional plots with results for the 25 photon per subaperture cases and the percentage changes in OTF are included in the appendix.

The overall implication of the OTF results is that the significant DM misalignments can be tolerated without significant loss in information content. The performance impact is very dependent upon atmospheric conditions, independent of object brightness, and slightly dependent upon the system response time. To further explore the impact of the information loss due to misalignment, the radial-averaged image spectrum SNR is now presented for the same cases.

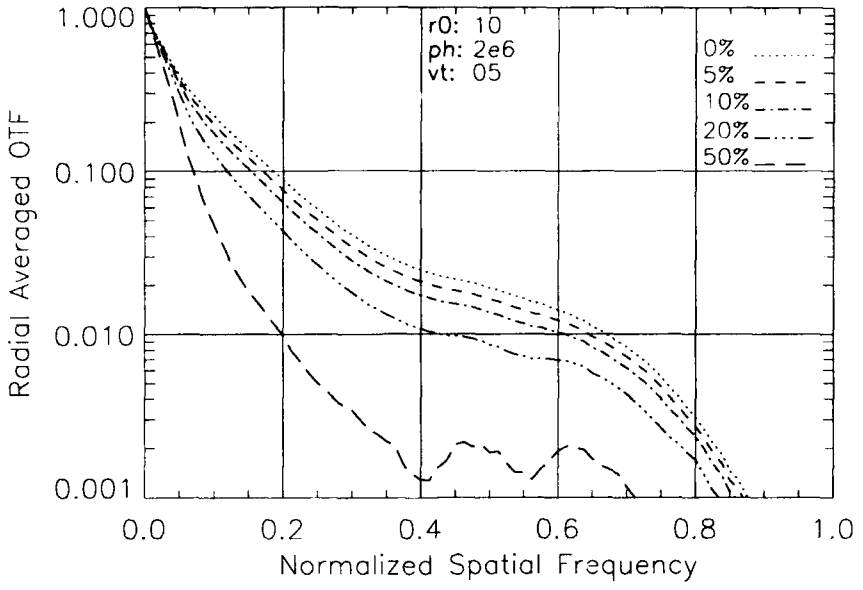

Figure 4-13 Misalignment Effects: Radial-Averaged OTF ($r_0 = 10$, $ph = 2\times10^6$, $v\tau = 05$)

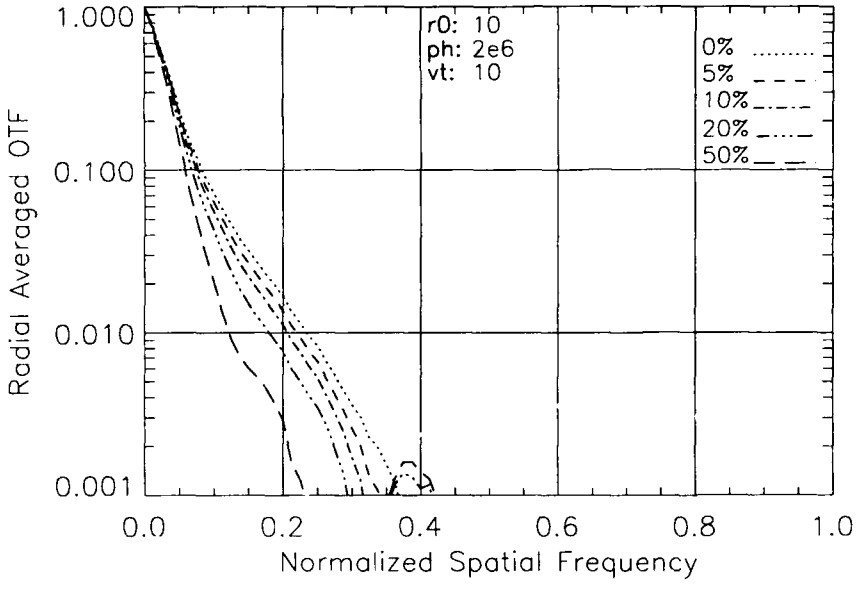

Figure 4-14 Misalignment Effects: Radial-Averaged OTF ($r_0 = 10$, $ph = 2\times10^6$, $v\tau = 10$)

Signal-to-Noise Ratio.

In order to account for the variance in the OTF, the image spectrum SNR of the system, with a star as the input object, was generated as a measure of AO system performance. Once again, the actual numbers vary significantly with seeing conditions, but degrade consistently from the perfect alignment cases. Overall the system is insensitive to the misalignments if the seeing conditions are good enough and the misalignments are small compared to the Fried parameter.

Figures 4-15, 4-17, 4-19 show that the SNR curves for the 5 percent misalignment cases are virtually indistinguishable from the perfect alignment cases. Additionally, the 5 percent and 10 percent misalignments are always less than 5 percent from the baseline SNR. The figures also indicate the same difference in cut-off frequencies, for differing Fried parameters, observed in the average OTF plots (Figures 4-2, 4-4, and 4-6). Overall the SNR results confirm the OTF results.

Figures 4-16, 4-18, and 4-20 show the percentage change in SNR is dependent upon atmospheric conditions. The impacts become worse as the Fried parameter drops and approach the value of the misalignments. Figures 4-17, 4-21, and 4-22 indicate that the SNR is slightly dependent upon the system response time. Although the curves drop as the time delay is increased, they remain relatively indistinguishable for all but the 50 percent misalignment. The SNR results confirm that significant DM misalignments can be tolerated without significant loss in information content.

The following figures show the radially averaged SNR and the percentage change from the baseline SNR for the 2,000,000 photons per subaperture cases at r_0 of 7, 10, and 13 cm. Additional plots for the 25 photons per subaperture cases are included in the appendix.

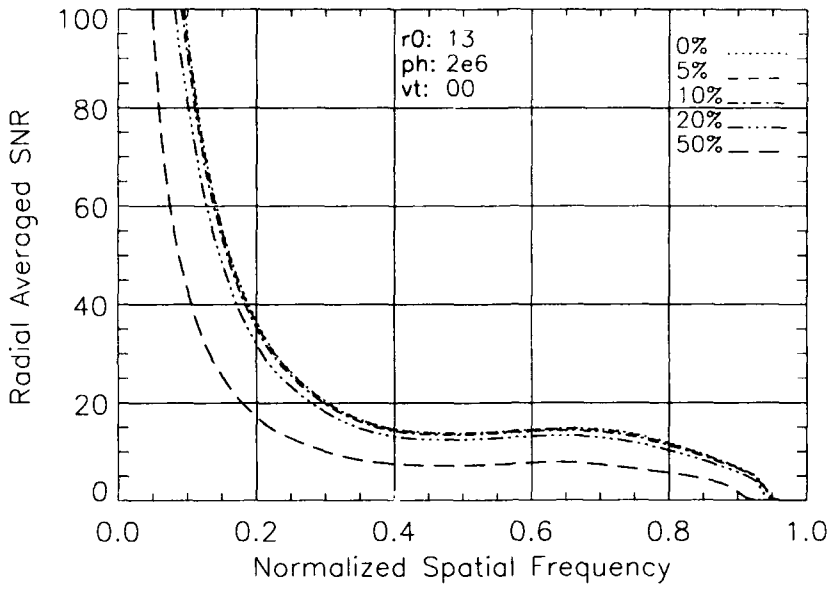

Figure 4-15 Misalignment Effects on Star Image SNR ($r_0 = 13$, $ph = 2\times10^6$, $v\tau = 0$)

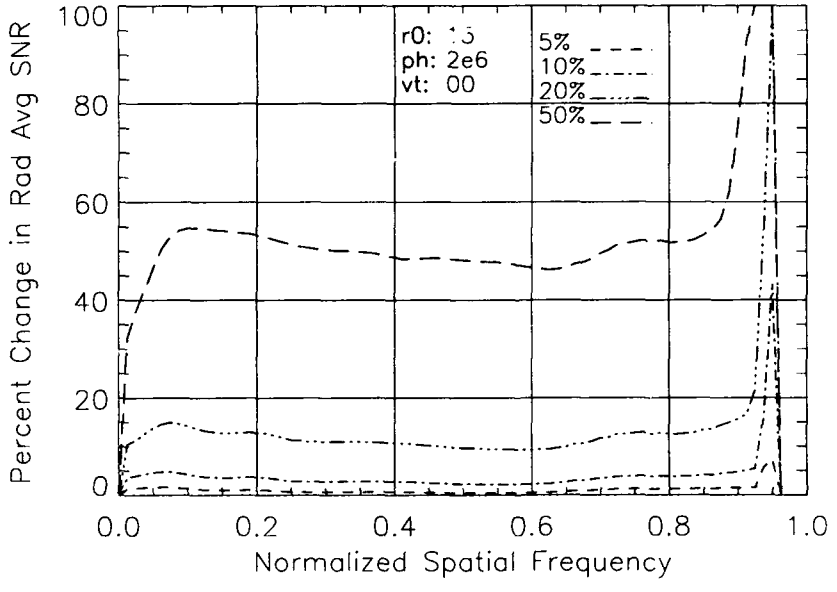

Figure 4-16 Misalignment Effects: Star Image SNR Change ($r_0 = 13$, $ph = 2\times10^6$, $v\tau=0$)

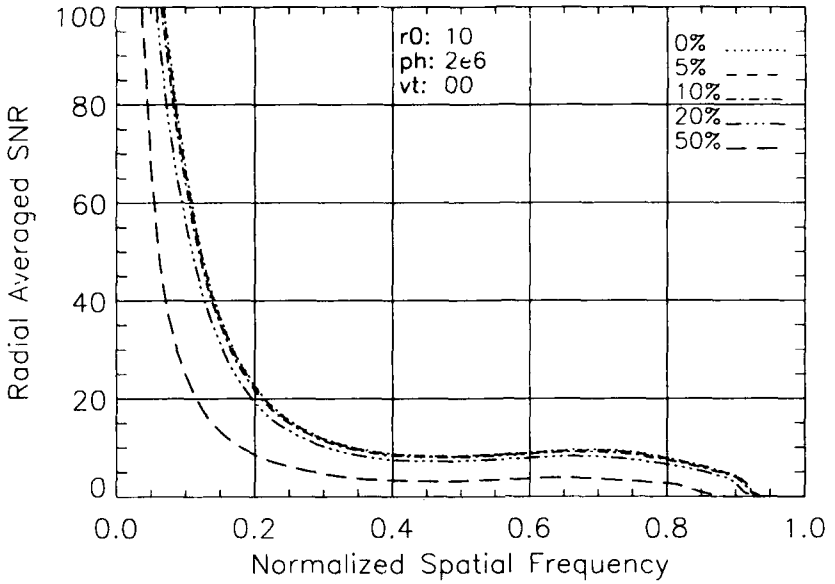

Figure 4-17 Misalignment Effects on Star Image SNR ($r_0 = 10$, $ph = 2\times10^6$, $v\tau = 0$)

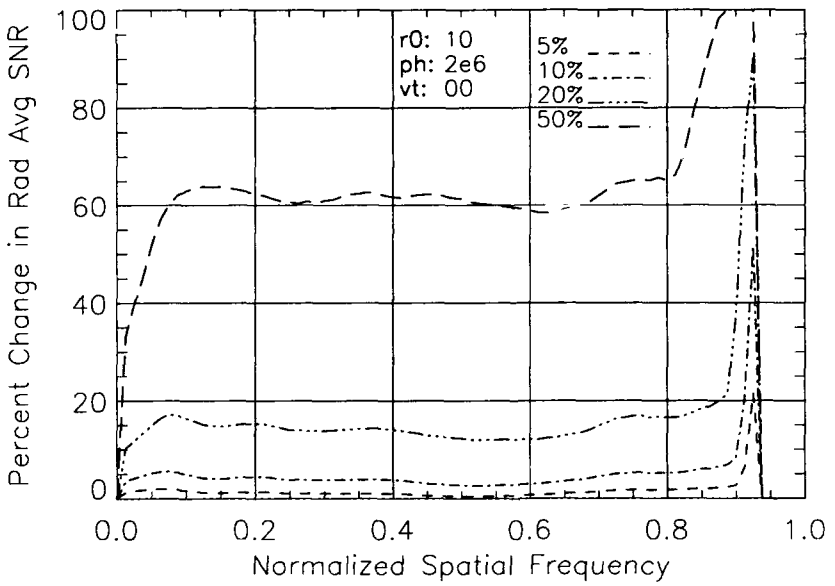

Figure 4-18 Misalignment Effects: Change ($r_0 = 10$, $ph = 2\times10^6$, $v\tau=0$)

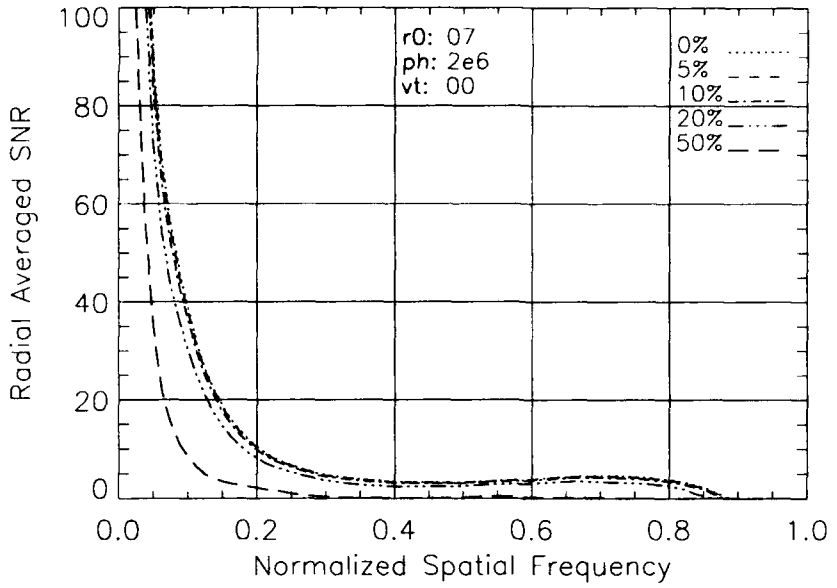

Figure 4-19 Misalignment Effects on Star Image SNR ($r_0 = 07$, $ph = 2\times10^6$, $v\tau = 0$)

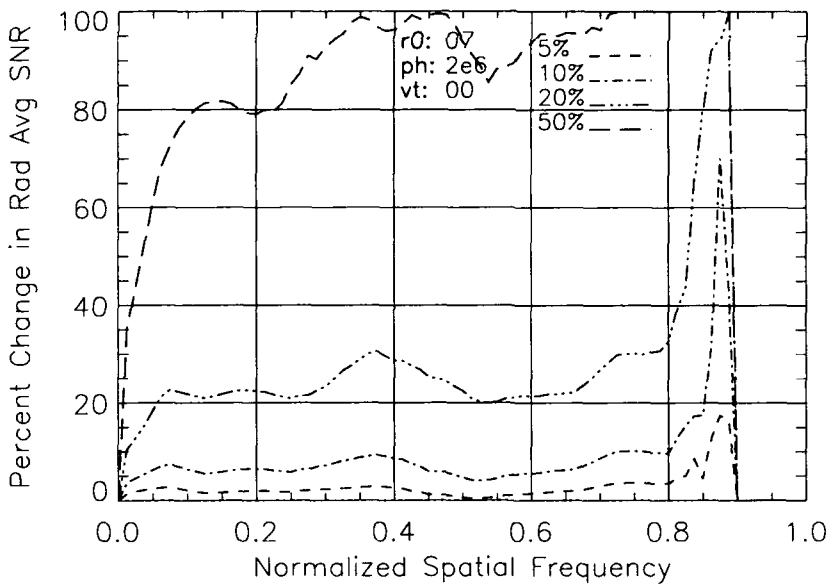

Figure 4-20 Misalignment Effects: Change ($r_0 = 07$, $ph = 2\times10^6$, $v\tau=0$)

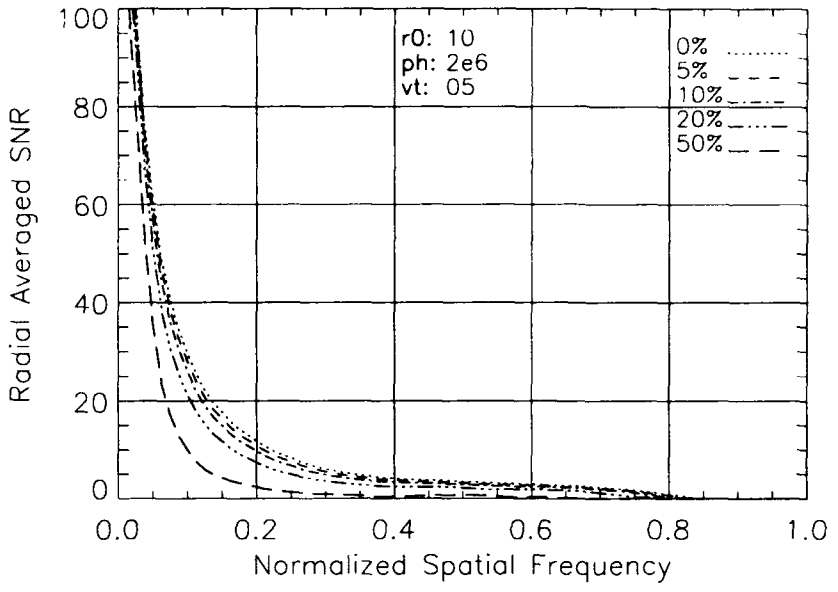

Figure 4-21 Misalignment Effects on Star Image SNR ($r_0 = 10$, $ph = 2\times10^6$, $v\tau = 05$)

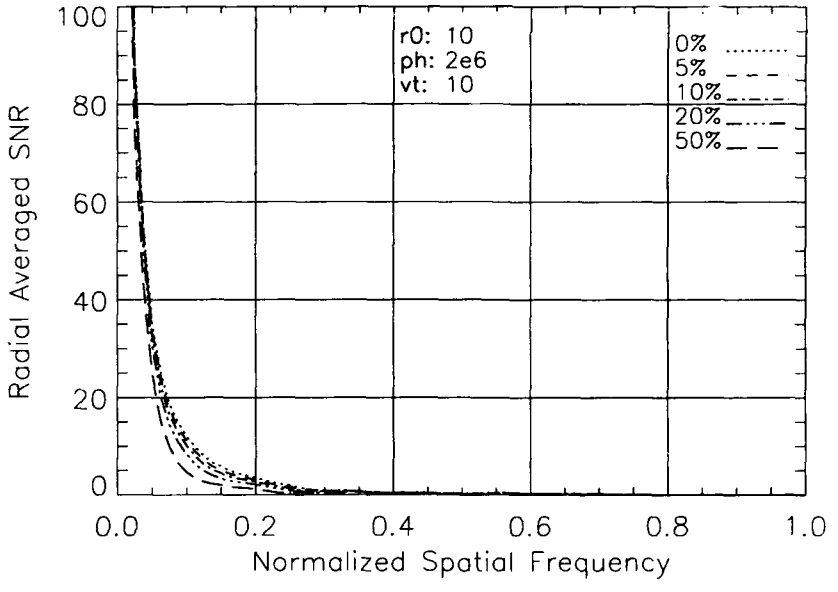

Figure 4-22 Misalignment Effects on Star Image SNR ($r_0 = 10$, $ph = 2\times10^6$, $v\tau = 10$)

Actuator Failure

The results of actuator failures upon AO performance are now presented. As previously stated, the system optical transfer function (OTF) and the system signal-to-noise ratio (SNR) are used to characterize the overall system performance.

Optical Transfer Function.

The OTF provides a measure of overall system throughput as a result of the phase corrections applied by the deformable mirror. The following figures show the radially averaged OTFs plotted versus normalized spatial frequency. Additionally, plots of the percentage change in the OTF relative to the no-failure cases are shown to better quantify the effects relative to the baseline. It is clear that the effects of actuator failure are gradual since performance degrades gracefully. The system is less sensitive to failure when seeing conditions are good than when they are poor. In all cases, system performance appears to be affected significantly only for failure of greater than 10 percent of the actuators.

Comparison of the 7-cm, 10-cm, and 13-cm Fried parameter cases in Figures 4-24, 4-26, and 4-28, shows that the percentage loss of information significantly increases as the atmospheric conditions degrade. At the relatively good seeing conditions of r_0 = 13 and 10 cm, the 5 percent actuator failure cases are within 5 percent of the baseline OTF. With conditions at r_0 = 7 cm, the loss of information increases to more than 10 percent of the baseline. This dependence upon the Fried parameter results from the fact that the incident wavefront is more highly corrupted for poorer seeing conditions. Since the failed actuators have been removed, there are fewer actuators available to apply the necessary correction. This results in a lower OTF for the system.

Additionally, as the average actuator separation of the remaining actuators approaches the Fried parameter, the performance degrades rapidly. For r_0 = 7 cm, the 50 percent curve has a much lower cut-off frequency, about 0.30, than the other curves,

about 0.9. At r_0 = 13 cm, the cut-off frequency for the 50 % curve is 0.90, while other curves cut-off at 0.95. This difference in cut-off frequencies is due to the relationship between the Fried parameter and the actuator separation. At r_0 = 7 cm, the 50 percent failure case corresponds to an *actsep* = 0.55 cm (80 percent of the r_0 value), while at r_0 = 13 cm, the 50 percent failure case (*actsep* = 0.55 cm) corresponds to only 40 percent of the r_0 value. As the actuator separation approaches the Fried parameter, the AO compensation becomes ineffective.

Comparison of the 2,000,000 photons per subaperture cases in Figures 4-23, 4-25, and 4-27 with the 25 photons per subaperture cases in Figures 4-29, 4-31, and 4-33, respectively, indicates that the performance impact of failures is dependent upon object brightness. There is a consistent spreading of the OTF curves as the brightness is decreased indicating that images of dimmer objects will be most affected by actuator failures. The major effect of object brightness on the AO system is the WFS SNR and thus the WFS measurement accuracy. Since there are fewer actuators available to apply the necessary corrections, the accuracy of the correction is reduced. The introduction of the increased measurement error, by dropping from *ph* of 2,000,000 to 25, compounds this effect, reducing the correction accuracy and the resulting OTF.

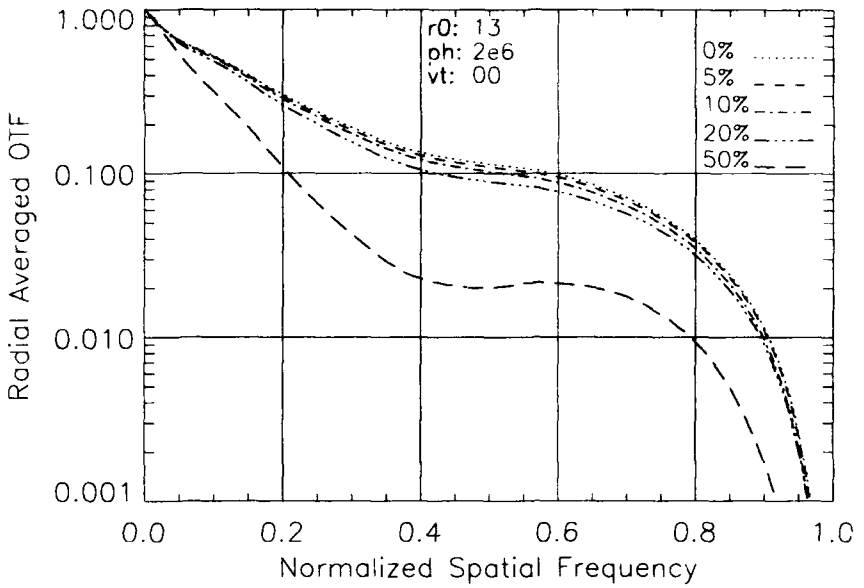

Figure 4-23 Failure Effects on Radially Avg OTF ($r_0 = 13$, $ph = 2\times10^6$, $v\tau = 0$)

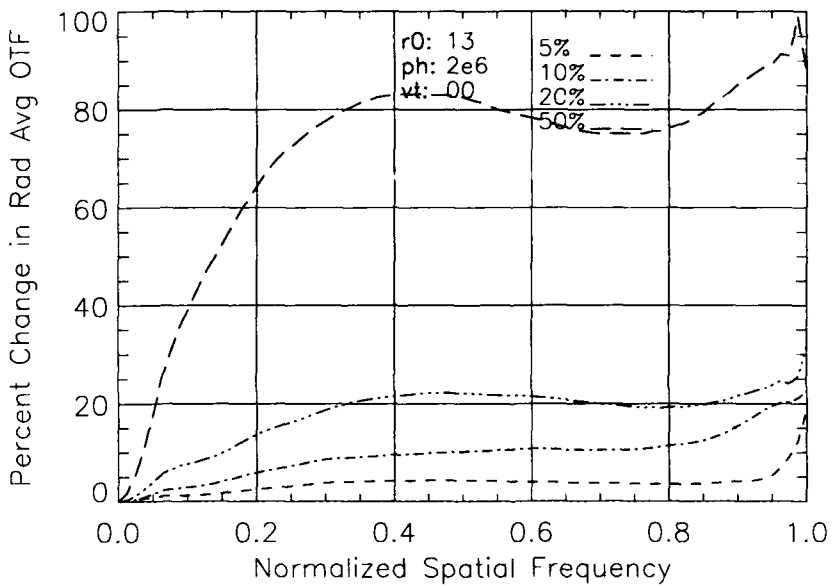

Figure 4-24 Failure Effects on Change in Avg OTF ($r_0 = 13$, $ph = 2\times10^6$, $v\tau = 0$)

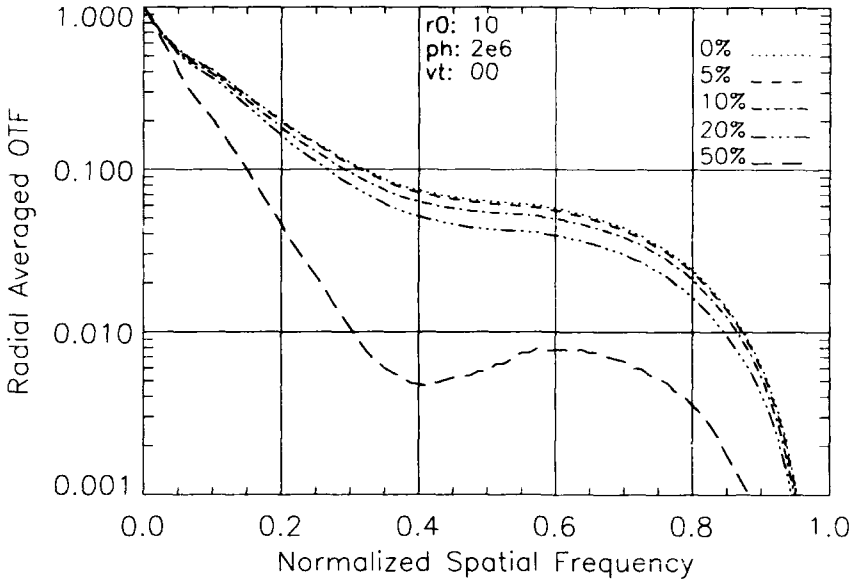

Figure 4-25 Failure Effects on Radially Avg OTF ($r_0 = 10$, $ph = 2\times10^6$, $v\tau = 0$)

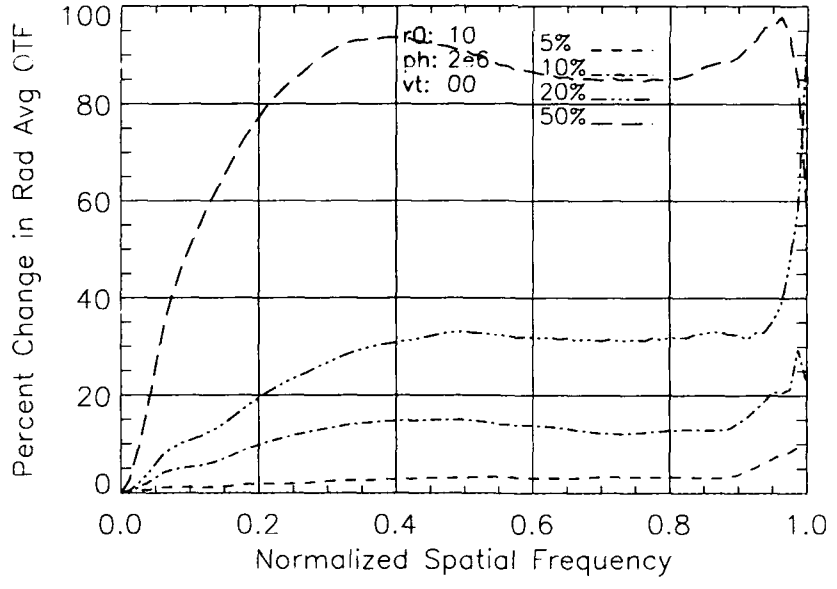

Figure 4-26 Failure Effects on Change in Avg OTF ($r_0 = 10$, $ph = 2\times10^6$, $v\tau = 0$)

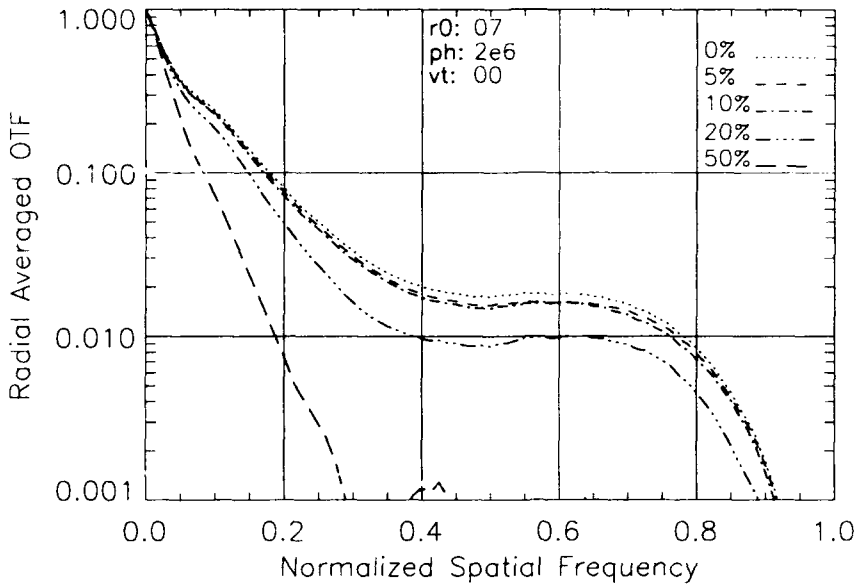

Figure 4-27 Failure Effects on Radially Avg OTF ($r_0 = 07$, $ph = 2\times10^6$, $v\tau = 0$)

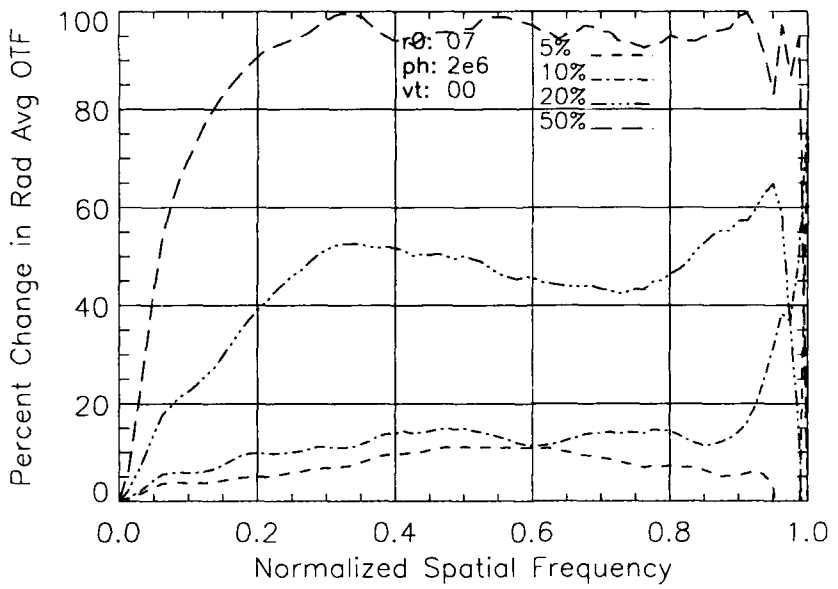

Figure 4-28 Failure Effects on Change in Avg OTF ($r_0 = 07$, $ph = 2\times10^6$, $v\tau = 0$)

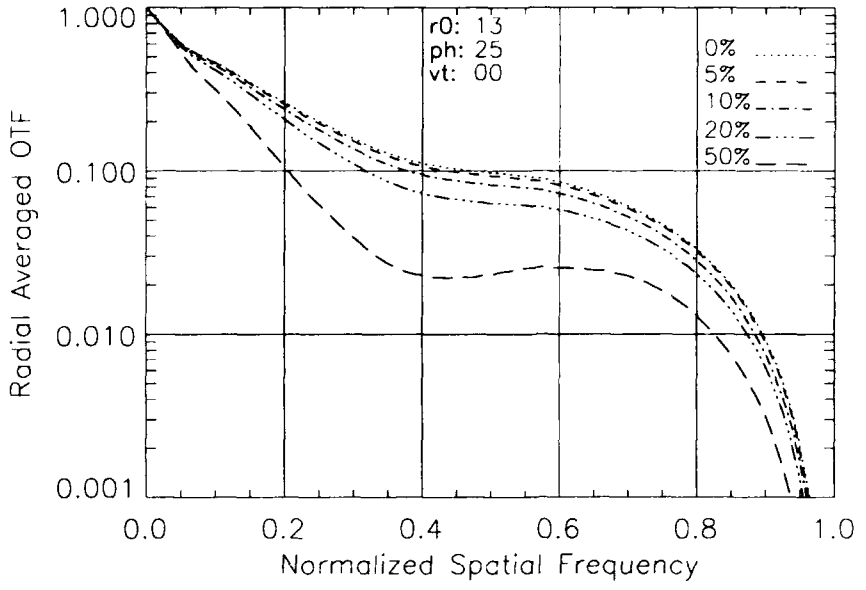

Figure 4-29 Failure Effects on Radially Avg OTF ($r_0 = 13$, $ph = 25$, $v\tau = 0$)

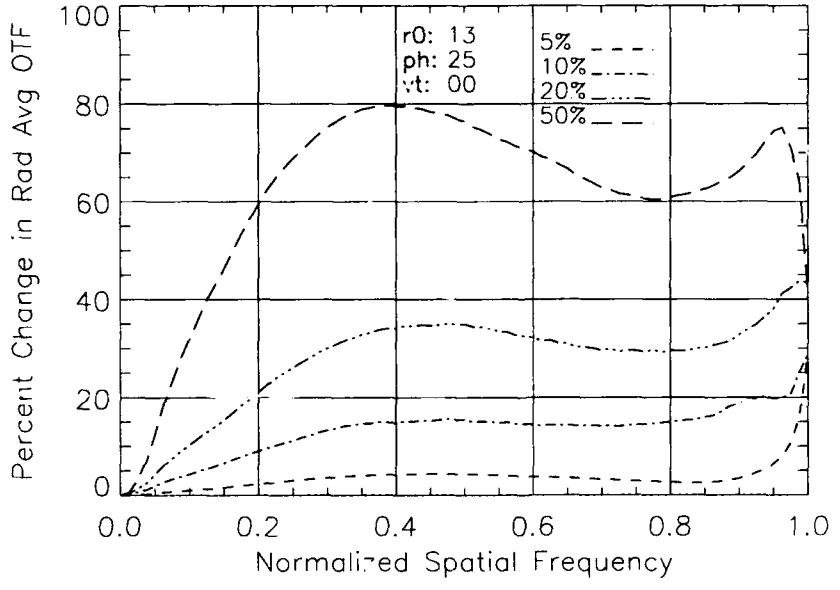

Figure 4-30 Failure Effects on Change in Avg OTF ($r_0 = 13$, $ph = 25$, $v\tau = 0$)

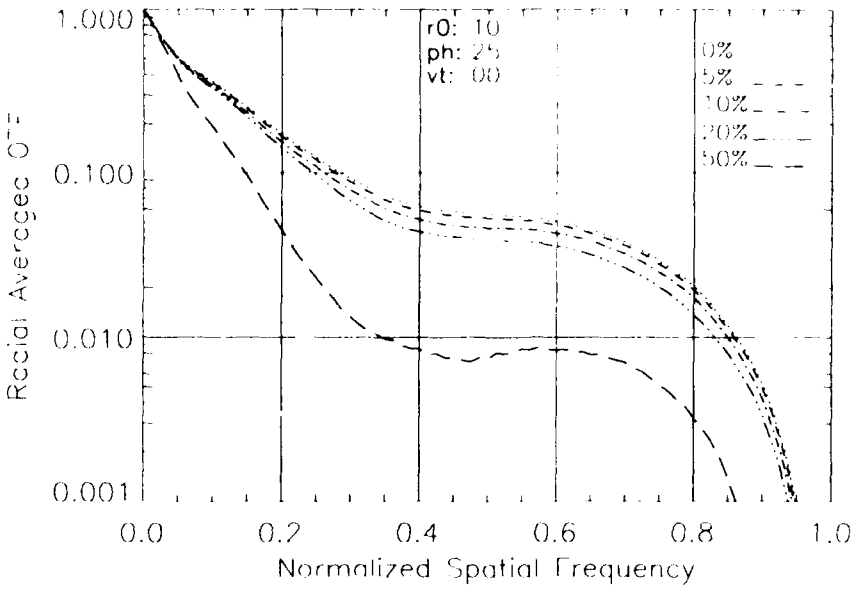

Figure 4-31 Failure Effects on Radially Avg OTF ($r_0 = 10$, $ph = 25$, $v\tau = 0$)

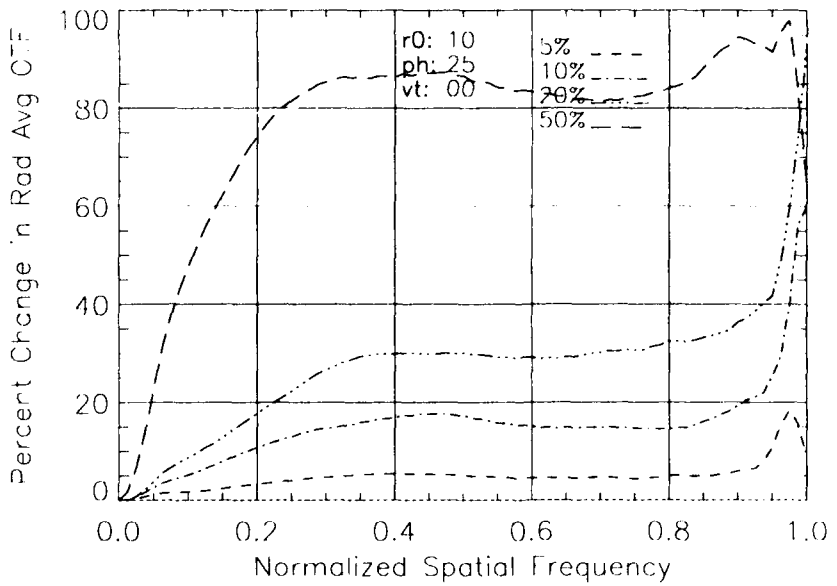

Figure 4-32 Failure Effects on Change in Avg OTF ($r_0 = 10$, $ph = 25$, $v\tau = 0$)

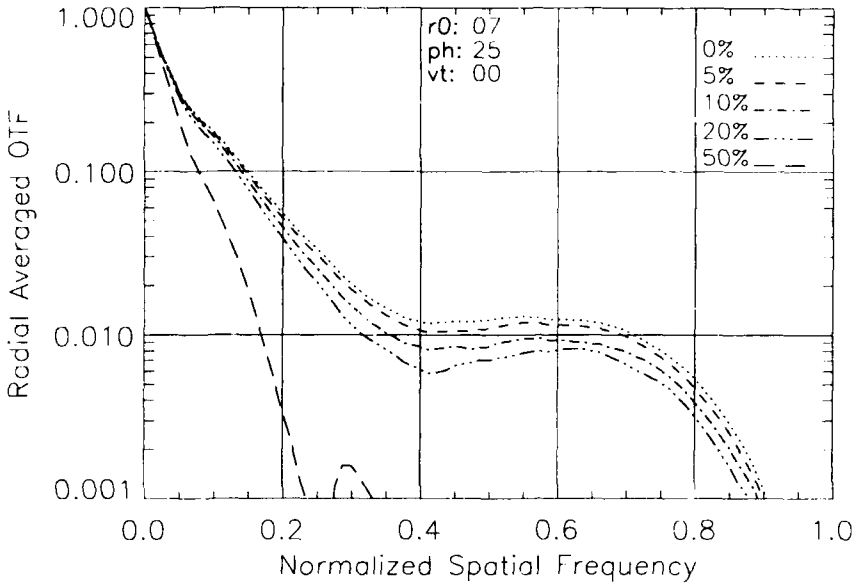

Figure 4-33 Failure Effects on Radially Avg OTF ($r_0 = 07$, $ph = 25$, $v\tau = 0$)

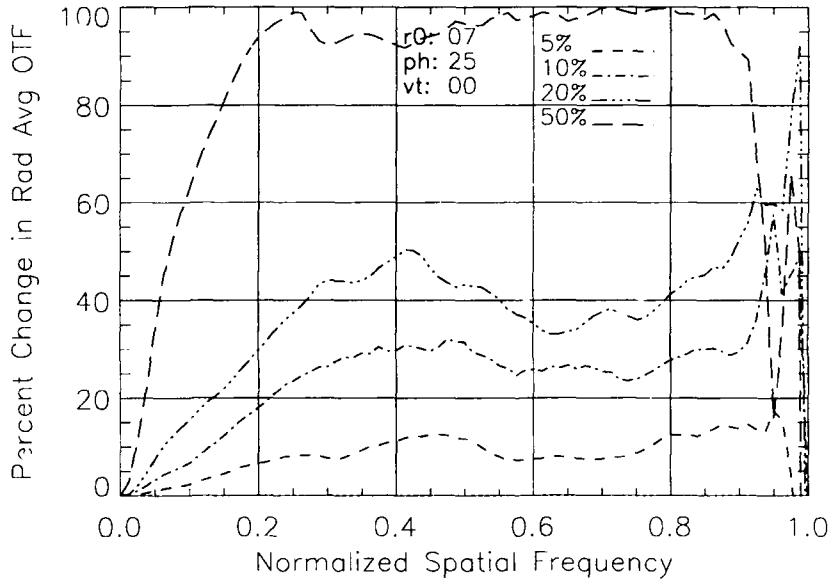

Figure 4-34 Failure Effects on Change in Avg OTF ($r_0 = 07$, $ph = 25$, $v\tau = 0$)

The effects of the actuator failures as related to system time delays ($\nu\tau$), are shown in the Figures 4-25, 4-35, and 4-36. They indicate that the failures will affect these systems in much the same way as the systems with instantaneous correction. The overall OTF drops significantly with increased time delays, but the percentage changes in OTFs are very similar to those of the instantaneous response cases. The OTFs begin to converge as the time delay increases, indicating that the impact of the failures is less in magnitude than the impact of the time delays. The failures still impact the overall performance gradually and predictably. Additional plots with results for the 25 photon per subaperture cases and the percentage changes in OTF are included in the appendix.

The overall implication of the OTF results is that significant percentages of failed actuators can be tolerated without significant loss in performance. The performance impact, relative to the baseline value, is very dependent upon atmospheric conditions, somewhat dependent upon object brightness, and virtually independent of the system response time. The relative dependence upon the various parameters indicates the relative magnitude of the impact of the failures vs the impact of the change in the parameters themselves. To further explore the impact of the information loss due to actuator failure, we now look at the radially averaged image spectrum SNR for the same cases.

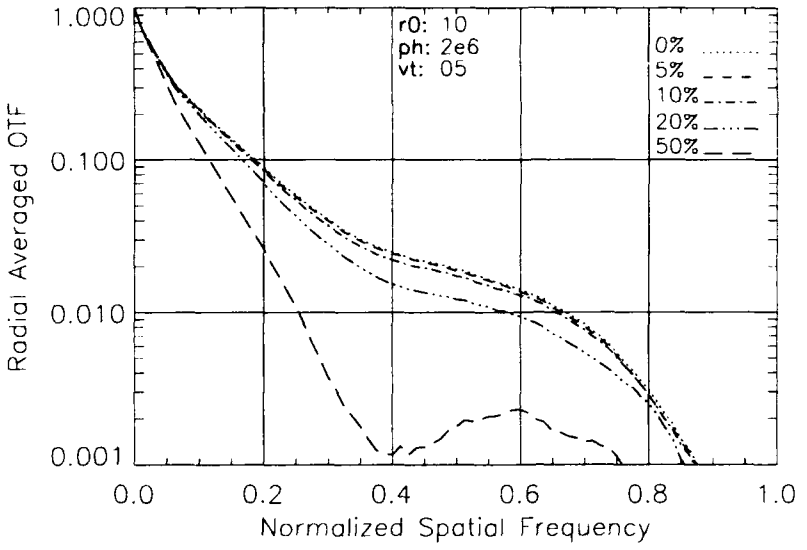

Figure 4-35 Failure Effects on Radially Avg OTF ($r_0 = 10$, $ph = 2\times10^6$, $v\tau = 05$)

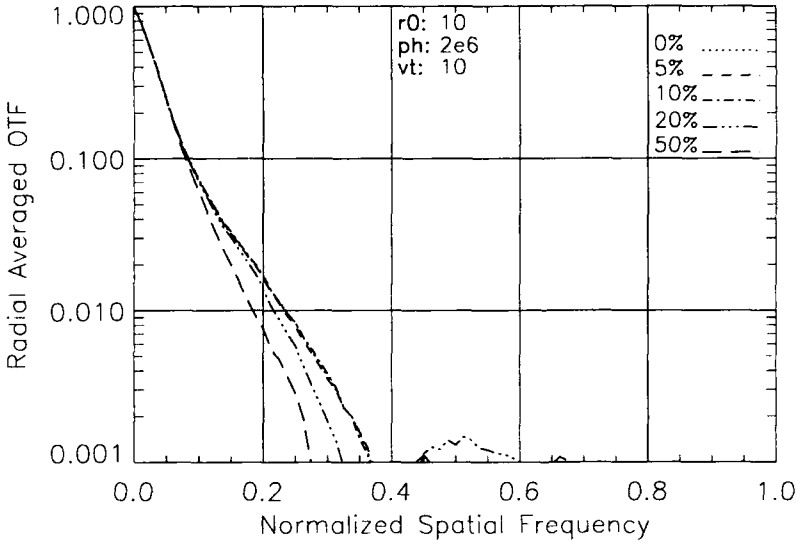

Figure 4-36 Failure Effects on Radially Avg OTF ($r_0 = 10$, $ph = 2\times10^6$, $v\tau = 10$)

Signal-to-Noise Ratio.

In order to account for the variance in the OTF, the SNR of the system was considered as a measure of AO system performance. Once again, the actual numbers vary

significantly with seeing conditions, but degrade consistently from the zero-failure cases. The trends confirm that the performance is somewhat predictable for varying actuator failures as well as seeing conditions. Overall, the system is insensitive to small percentage failures if the seeing conditions are good enough.

Figures 4-37, 4-39, 4-41 show that the SNR curves for the 5 percent failure cases are very close to the zero failure cases. Additionally, Figures 4-38, 4-40, and 4-42 show that the 5 percent and 10 percent misalignments are always less than 5 percent from the baseline SNR. The figures also indicate the same difference in cut-off frequencies, for differing Fried parameters, observed in the average OTF plots Figures 4-24, 4-26, and 4-28. Overall the SNR results confirm the OTF results.

Figures 4-38, 4-40, and 4-42 show the percentage change in SNR is dependent upon atmospheric conditions. The impacts become worse as the Fried parameter drops and approaches the average actuator separation. Figures 4-39, 4-43, and 4-44 indicate that the SNR is dependent upon the system response time. As the curves drop with increased time delay, they become less distinguishable, indicating that the impact of the failures is less in magnitude than the impact of the time delays. The SNR results confirm that significant DM misalignments can be tolerated without significant loss in performance. Overall the SNR results are consistent with the OTF results. Additionally, since the actuator failures were applied randomly, the exact spacing of actuators was not constant. The system appears to be insensitive to this type of error since the OTF and SNR plots remained relatively smooth and predictable.

The following figures show the radially averaged SNR and the percentage change from the baseline SNR for the 2,000,000 photons per subaperture cases at r_0 of 7, 10, and 13 cm. Additional plots for the 25 photons per subaperture cases are included in the appendix.

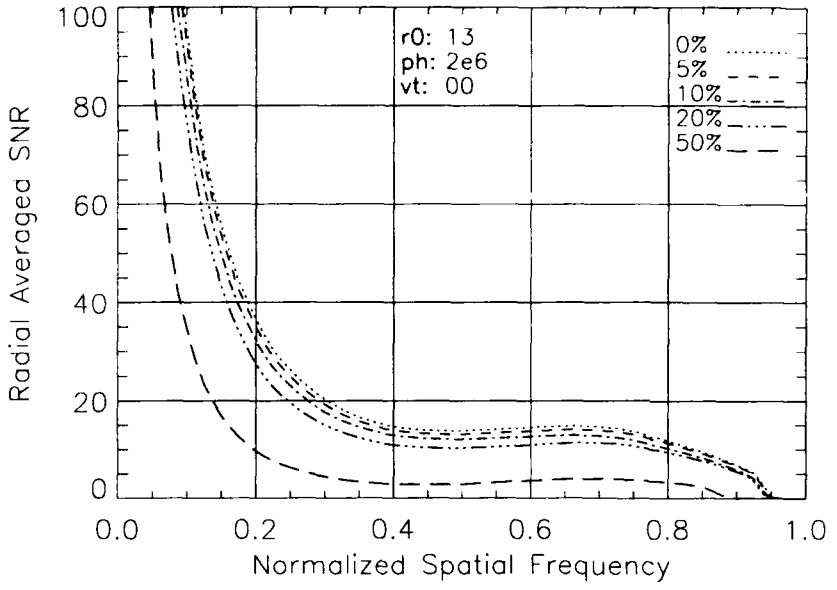

Figure 4-37 Failure Effects on Star Image SNR ($r_0 = 13$, $ph = 2\times10^6$, $v\tau = 0$)

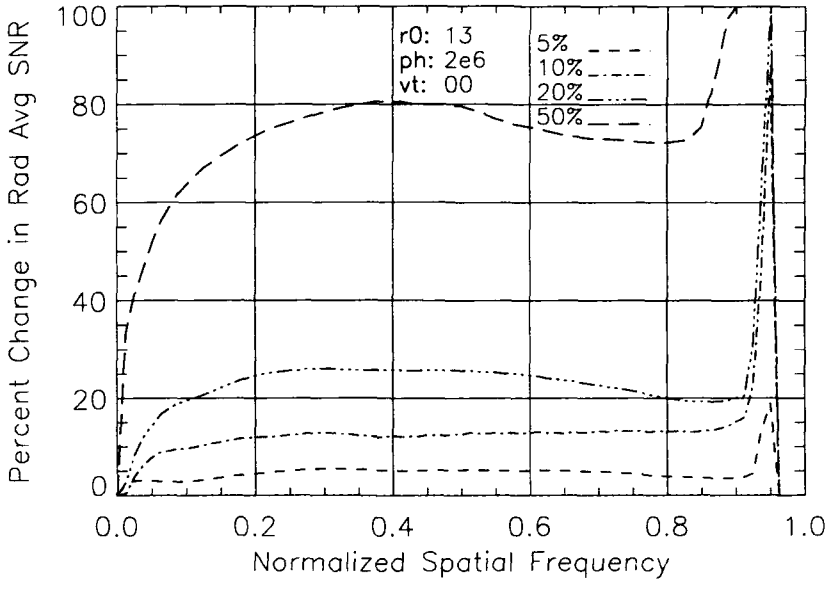

Figure 4-38 Failure Effects on Change in Star Image SNR ($r_0 = 13$, $ph = 2\times10^6$, $v\tau = 0$)

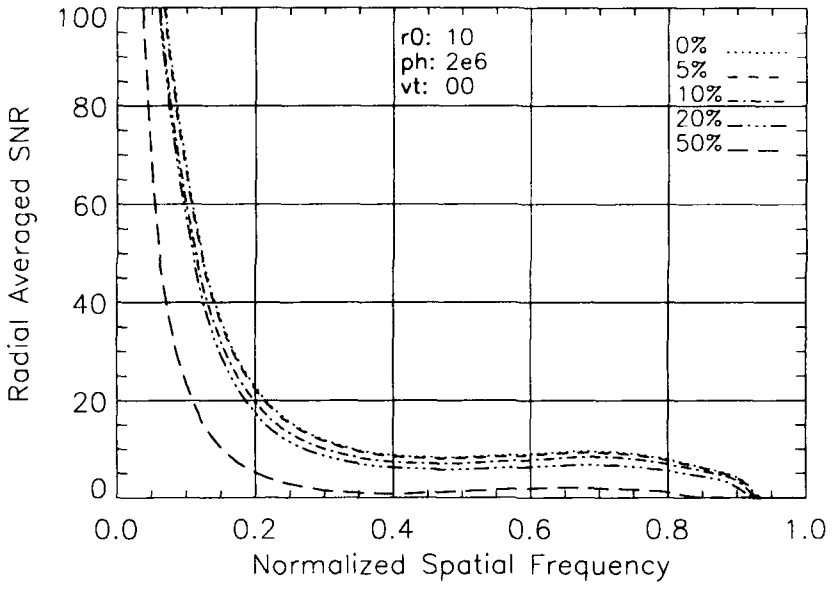

Figure 4-39 Failure Effects on Star Image SNR ($r_0 = 10$, $ph = 2\times10^6$, $v\tau = 0$)

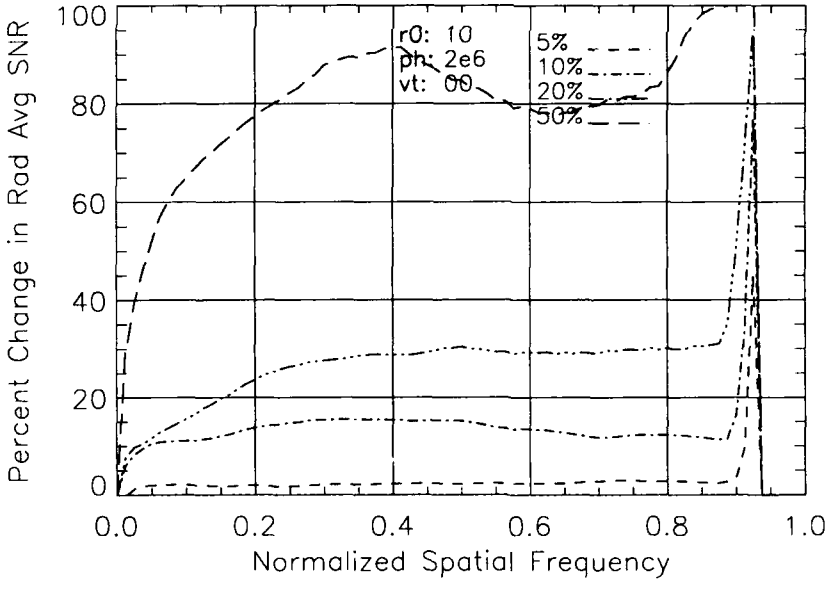

Figure 4-40 Failure Effects on Change in Star Image SNR ($r_0 = 10$, $ph = 2\times10^6$, $v\tau = 0$)

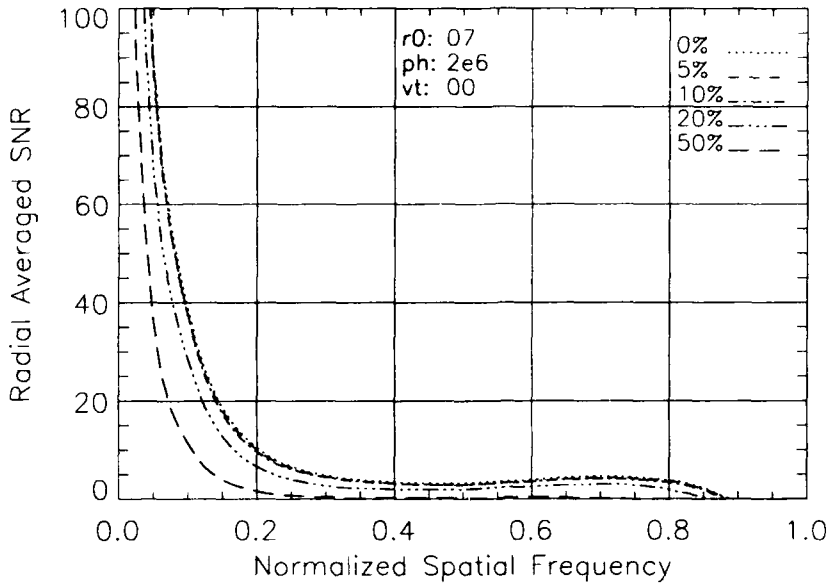

Figure 4-41 Failure Effects on Star Image SNR ($r_0 = 07$, $ph = 2\times10^6$, $v\tau = 0$)

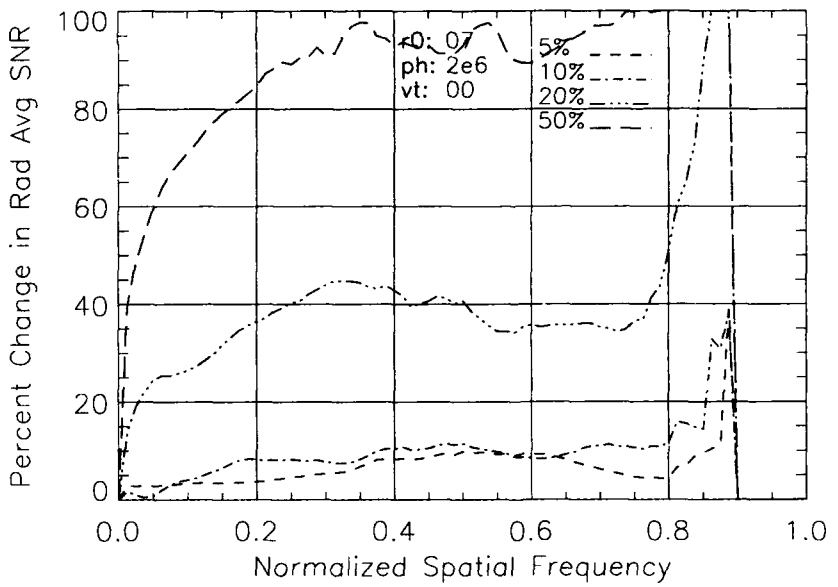

Figure 4-42 Failure Effects on Change in Star Image SNR ($r_0 = 07$, $ph = 2\times10^6$, $v\tau = 0$)

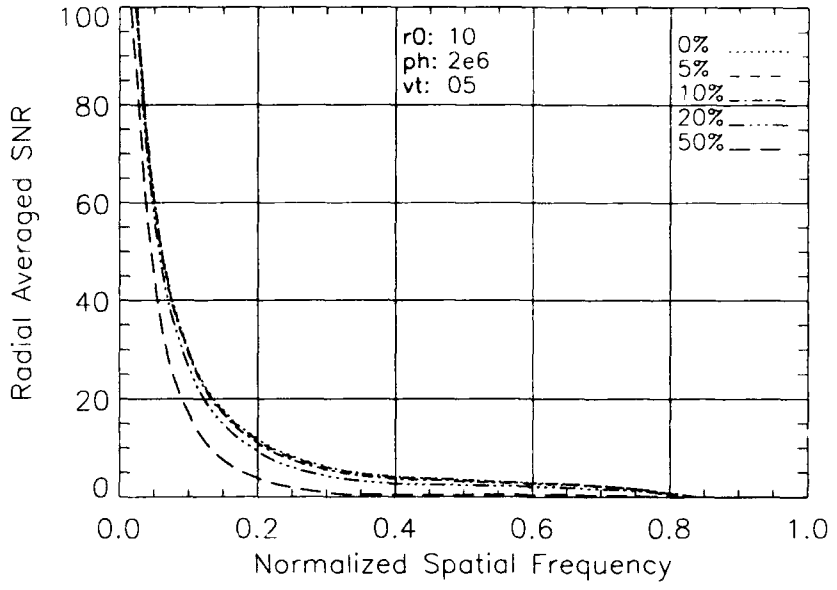

Figure 4-43 Failure Effects on Star Image SNR ($r_0 = 10$, $ph = 2\times10^6$, $v\tau = 05$)

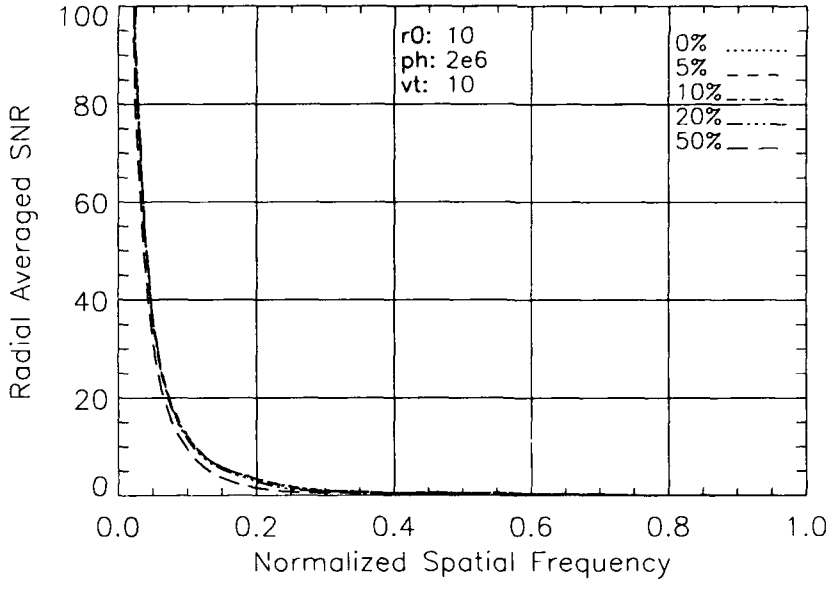

Figure 4-44 Failure Effects on Star Image SNR ($r_0 = 10$, $ph = 2\times10^6$, $v\tau = 10$)

Conclusions

The overall impact of the actuator misalignments and failures is graceful. The adaptive optics system is insensitive to actuator misalignments and failures if the seeing conditions are relatively good. Performance degradation increases as the seeing conditions deteriorate. While the system performance impacts appear to be very dependent upon the seeing conditions, they are less dependent upon object brightness and system time delay. The similarity in results among the 5 percent cases and the perfect-alignment cases suggests that a significant misalignment, on the order of 5 percent of the actuator separation (0.05×11 cm = 0.55 cm as projected into the pupil) will have little effect on performance. Similarly, a loss of 5 percent of the actuators should have minimal effect upon the system performance.

For all configurations, the performance impacts were dependent upon the relative value of the Fried parameter to the deformable mirror displacement for the misalignment cases, and the effective actuator spacing for the failure cases. The effects increase as the misalignment approaches the Fried parameter value, as well as when the average actuator spacing (due to loss of actuators) approaches the r_0 value. Not surprisingly, the performance of adaptive-optic systems with random actuator failure resembles that of reduced-actuator (partially-compensated) configurations. Techniques used to obtain high-spatial-resolution images from partially-compensated telescopes (7:4233) could be employed to compensate for the less than ideal configurations. In this way, the impact of failed actuators, and possibly misalignments, could be minimized.

V. CONCLUSIONS

The goal of this research was to characterize adaptive optics system performance relative to deformable mirror actuator misalignment and partial failure. This analysis provides information necessary for determining system specifications related to design, maintenance, and replacement of the deformable mirror. System performance has been evaluated using three measures:

- Mean-Square-Residual Phase Error,
- Optical Transfer Function, and
- Signal to Noise Ratio.

The overall effect of less than ideal configurations has been characterized as graceful degradation as shown by the consistency in both shape and magnitude of the OTF and SNR plots. The results indicate that the performance of the system is very stable when faced with small deviations from the baseline case. While the system performance impacts are very dependent upon the seeing conditions, they are less dependent upon object brightness and system time delay. The similarity in results among the 5 percent misalignment cases and the perfect-alignment cases suggests that a significant misalignment, on the order of 5 percent of the actuator separation (or 0.55 cm as projected into the pupil) will have little effect on performance. The impact increases as the misalignment approaches the Fried parameter value. Similarly, a loss of 5 percent of the actuators should have minimal effect upon the system performance. As the average actuator spacing approaches the r_0 value, due to loss of actuators, the performance impact increases. For all configurations, the performance impacts were dependent upon the relative value of the Fried parameter to the deformable mirror displacement for the misalignment cases, and the effective actuator spacing for the failure cases.

Not surprisingly, the performance of adaptive optic systems with random actuator failure resembles that of reduced-actuator (partially-compensated) configurations. The results indicate that the performance of an adaptive optics system is insensitive with regard to small actuator misalignments and failures. Additionally, these effects may be minimized through image reconstruction techniques. Depending upon expected seeing conditions and user requirements, this robust nature of the system should allow a relaxation of design specifications as well as maintenance and replacement schedules for the deformable mirrors of large aperture telescopes.

Future research is suggested to characterize the system performance when the failed actuators have not been removed. Analysis should be performed for the two possible failure cases not addressed in this research: failure without adjustment of the reconstruction matrix and failure with recalculation of the optimal matrix. This characterization will be needed to determine the optimal time for the DM to be removed and failed actuators removed. The operational impact of the necessary downtime should be compared to the impact of degraded system performance with continued operation.

Additional research is also suggested to extend the characterizations presented here. The impact of the misalignments and failures when coupled with more of the realistic operational considerations such as anisoplanatism, closed-loop control systems, and more extensive noise realizations should be considered.

Finally, it is recommended that these effects be coupled with a simulation of images of actual satellites, incorporating satellite characteristics (including relative sun-satellite-telescope location) with the atmospheric and adaptive optics effects. The generation of simulated images could be of great value in the training of AMOS/AEOS personnel.

APPENDIX

Variation of Parameters for Simulation Runs

Table A-1 Variable Parameters for Misalignment Runs

Misaligned Actuators			
r0 (cm)	*ph* (ph/sa)	$v\tau$ (cm)	*shift* (%)
7	2000000	0	0
7	2000000	0	5
7	2000000	0	10
7	2000000	0	20
7	2000000	0	50
7	100	0	0
7	100	0	5
7	100	0	10
7	100	0	20
7	100	0	50
7	25	0	0
7	25	0	5
7	25	0	10
7	25	0	20
7	25	0	50

Misaligned Actuators			
r0 (cm)	*ph* (ph/sa)	$v\tau$ (cm)	*shift* (%)
10	2000000	0	0
10	2000000	0	5
10	2000000	0	10
10	2000000	0	20
10	2000000	0	50
10	100	0	0
10	100	0	5
10	100	0	10
10	100	0	20
10	100	0	50
10	25	0	0
10	25	0	5
10	25	0	10
10	25	0	20
10	25	0	50

Table A-1 (cont) Variable Parameters for Misalignment Runs

Misaligned Actuators			
r0 (cm)	*ph* (ph/sa)	$v\tau$ (cm)	*shift* (%)
13	2000000	0	0
13	2000000	0	5
13	2000000	0	10
13	2000000	0	20
13	2000000	0	50
13	100	0	0
13	100	0	5
13	100	0	10
13	100	0	20
13	100	0	50
13	25	0	0
13	25	0	5
13	25	0	10
13	25	0	20
13	25	0	50

Table A-1 (cont) Variable Parameters for Misalignment Runs

Misaligned Actuators (with delay)			
r0 (cm)	*ph* (ph/sa)	$v\tau$ (cm)	*shift* (%)
10	2000000	5	0
10	2000000	5	5
10	2000000	5	10
10	2000000	5	20
10	2000000	5	50
10	2000000	10	0
10	2000000	10	5
10	2000000	10	10
10	2000000	10	20
10	2000000	10	50

Misaligned Actuators (with delay)			
r0 (cm)	*ph* (ph/sa)	$v\tau$ (cm)	*shift* (%)
10	25	5	0
10	25	5	5
10	25	5	10
10	25	5	20
10	25	5	50
10	25	10	0
10	25	10	5
10	25	10	10
10	25	10	20
10	25	10	50

Table A-2 Variable Parameters for Failure Runs

Failed Actuators			
r0 (cm)	*ph* (ph/sa)	$v\tau$ (cm)	*shift* (%)
7	2000000	0	0
7	2000000	0	5
7	2000000	0	10
7	2000000	0	20
7	2000000	0	50
7	100	0	0
7	100	0	5
7	100	0	10
7	100	0	20
7	100	0	50
7	25	0	0
7	25	0	5
7	25	0	10
7	25	0	20
7	25	0	50

Failed Actuators			
r0 (cm)	*ph* (ph/sa)	$v\tau$ (cm)	*shift* (%)
10	2000000	0	0
10	2000000	0	5
10	2000000	0	10
10	2000000	0	20
10	2000000	0	50
10	100	0	0
10	100	0	5
10	100	0	10
10	100	0	20
10	100	0	50
10	25	0	0
10	25	0	5
10	25	0	10
10	25	0	20
10	25	0	50

Table A-2 (cont) Variable Parameters for Failure Runs

Failed Actuators			
r0 (cm)	*ph* (ph/sa)	$v\tau$ (cm)	*shift* (%)
13	2000000	0	0
13	2000000	0	5
13	2000000	0	10
13	2000000	0	20
13	2000000	0	50
13	100	0	0
13	100	0	5
13	100	0	10
13	100	0	20
13	100	0	50
13	25	0	0
13	25	0	5
13	25	0	10
13	25	0	20
13	25	0	50

Table A-2 (cont) Variable Parameters for Failure Runs

Failed Actuators (with delay)			
r0 (cm)	*ph* (ph/sa)	$v\tau$ (cm)	*shift* (%)
10	2000000	5	0
10	2000000	5	5
10	2000000	5	10
10	2000000	5	20
10	2000000	5	50
10	2000000	10	0
10	2000000	10	5
10	2000000	10	10
10	2000000	10	20
10	2000000	10	50

Failed Actuators (with delay)			
r0 (cm)	*ph* (ph/sa)	$v\tau$ (cm)	*shift* (%)
10	25	5	0
10	25	5	5
10	25	5	10
10	25	5	20
10	25	5	50
10	25	10	0
10	25	10	5
10	25	10	10
10	25	10	20
10	25	10	50

Additional Misaligned Actuator Results

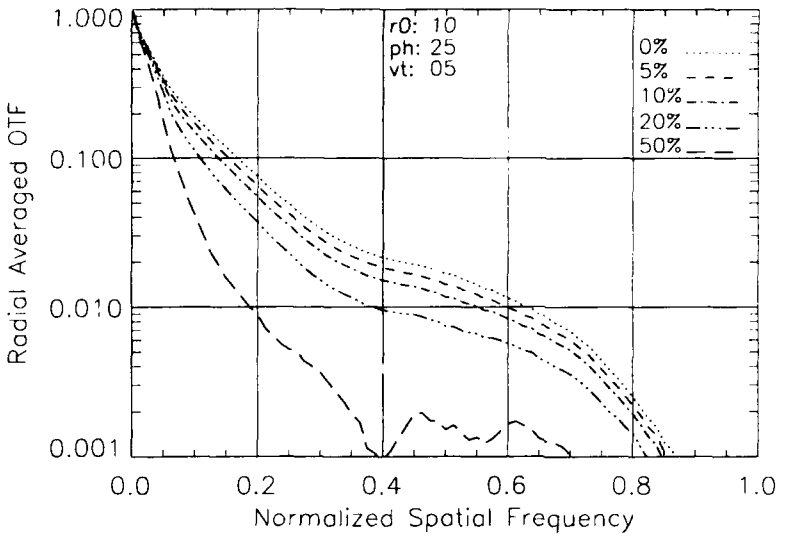

Figure A-1 Misalignment Effects on Radial-Averaged OTF ($r_0 = 10, ph = 25, v\tau = 05$)

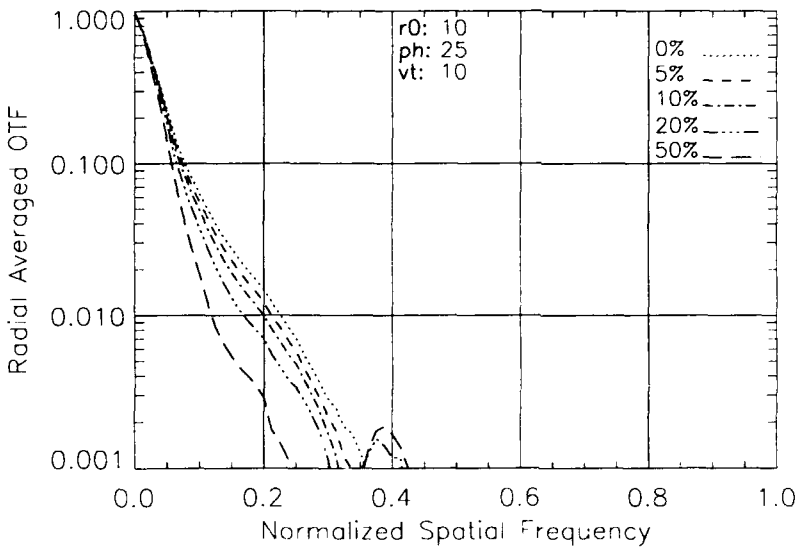

Figure A-2 Misalignment Effects on Radial-Averaged OTF ($r_0 = 10, ph = 25, v\tau = 10$)

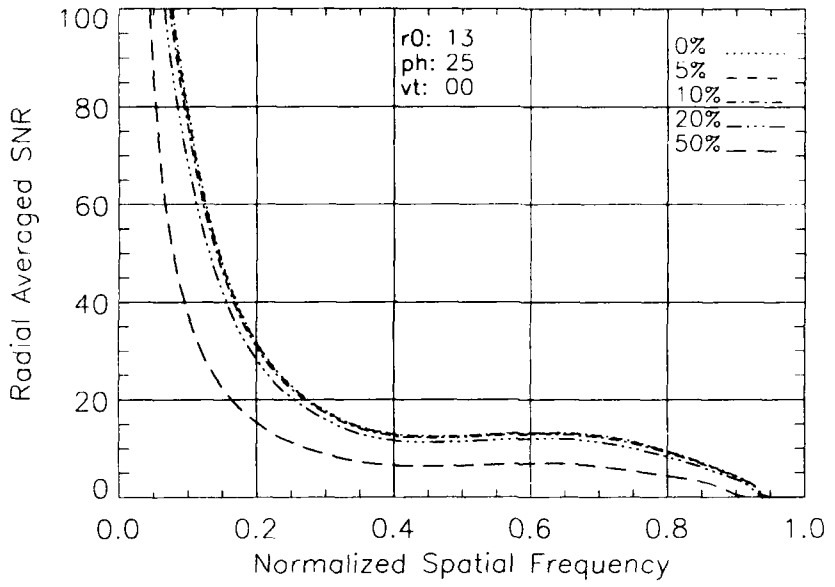

Figure A-3 Misalignment Effects on Radial-Averaged SNR ($r_0 = 13$, $ph = 25$, $v\tau = 00$)

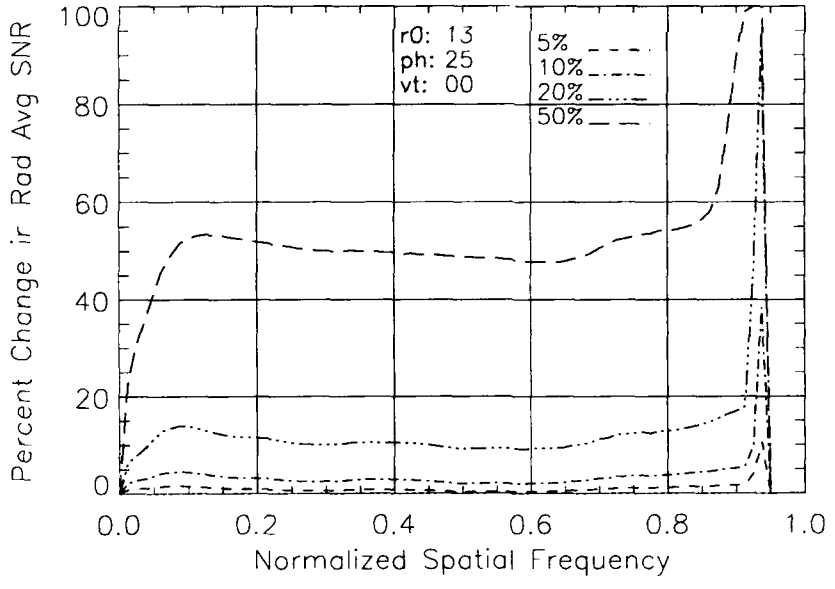

Figure A-4 Misalignment Effects on Change in Avg SNR ($r_0 = 13$, $ph = 25$, $v\tau = 00$)

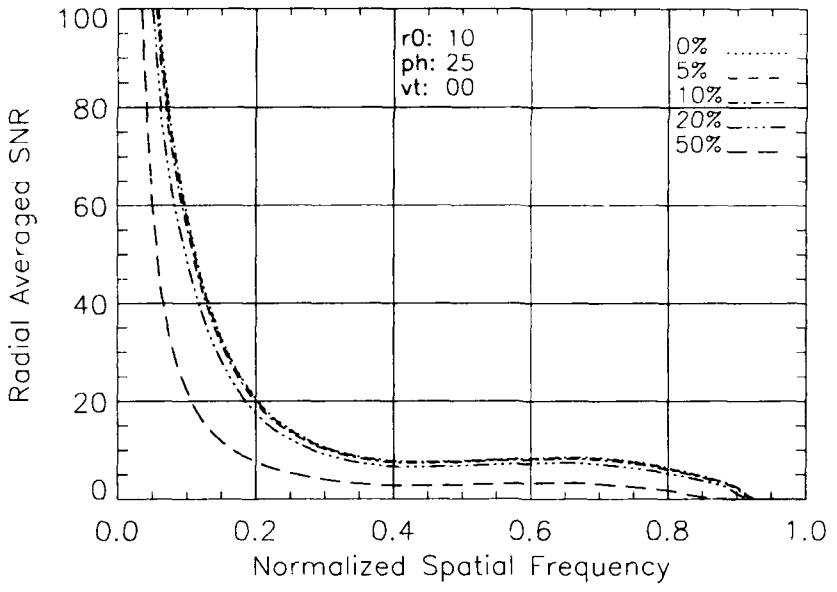

Figure A-5 Misalignment Effects on Radially Avg SNR ($r_0 = 10$, $ph = 25$, $v\tau = 00$)

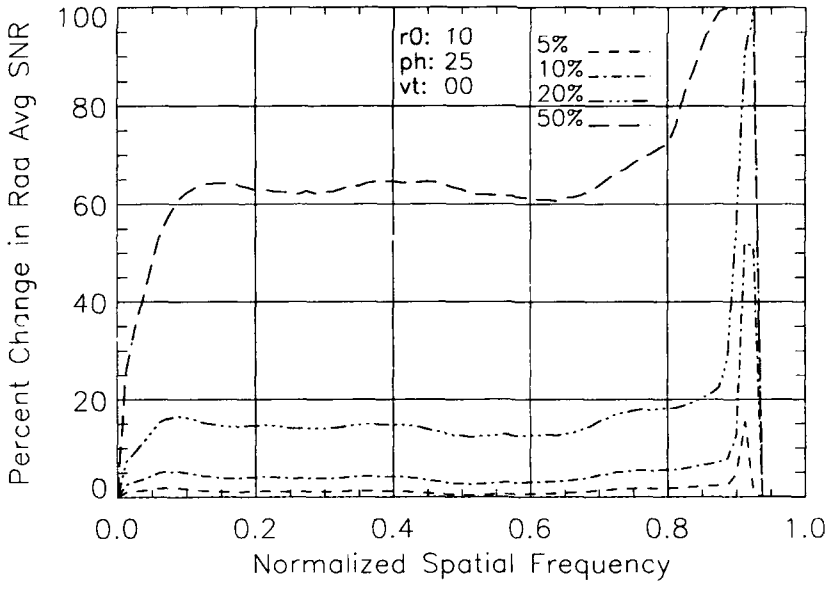

Figure A-6 Misalignment Effects on Change in Avg SNR ($r_0 = 10$, $ph = 25$, $v\tau = 00$)

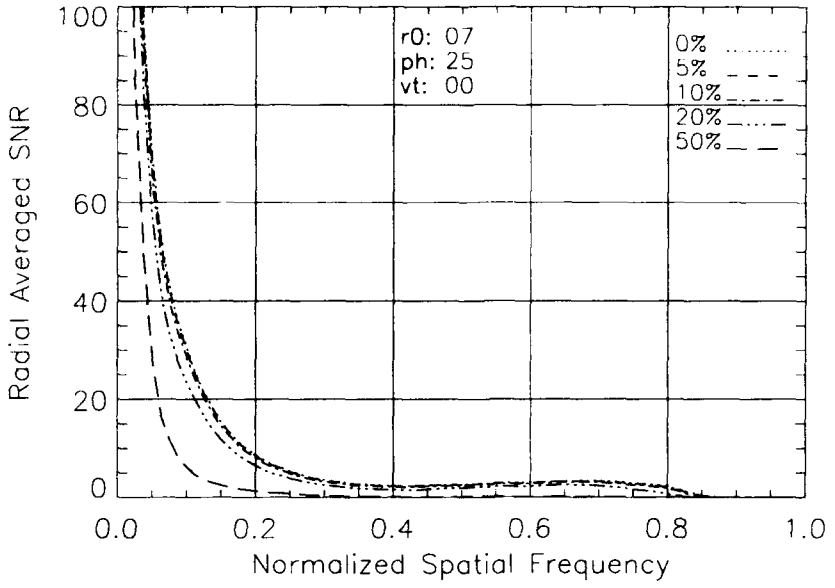

Figure A-7 Misalignment Effects on Radially Avg SNR ($r_0 = 07$, $ph = 25$, $v\tau = 00$)

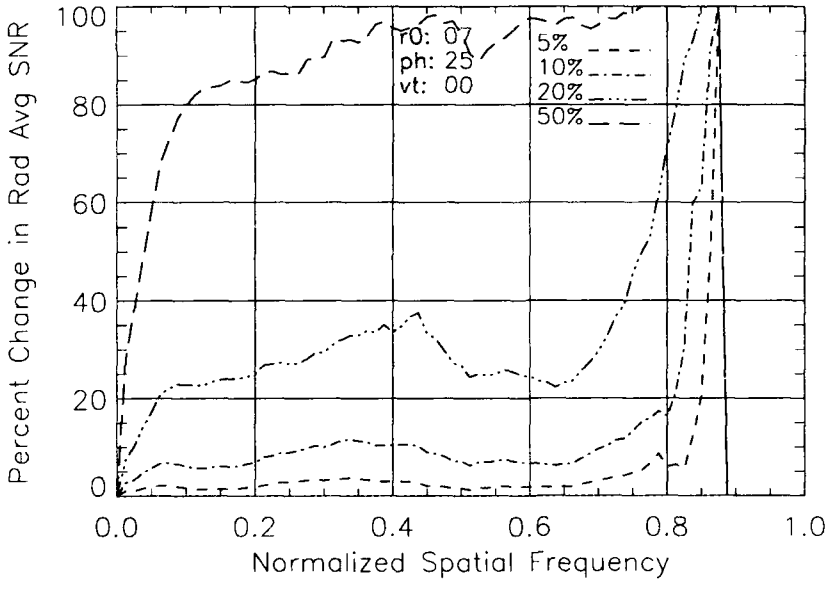

Figure A-8 Misalignment Effects on Change in Avg SNR ($r_0 = 07$ $ph = 25$, $v\tau = 00$)

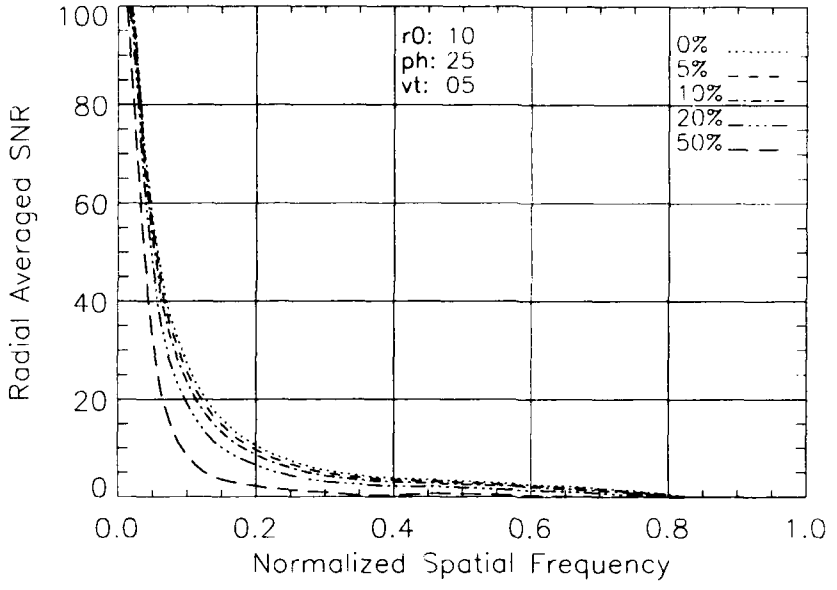

Figure A-9 Misalignment Effects on Radially Avg SNR ($r_0 = 10$, $ph = 25$, $v\tau = 05$)

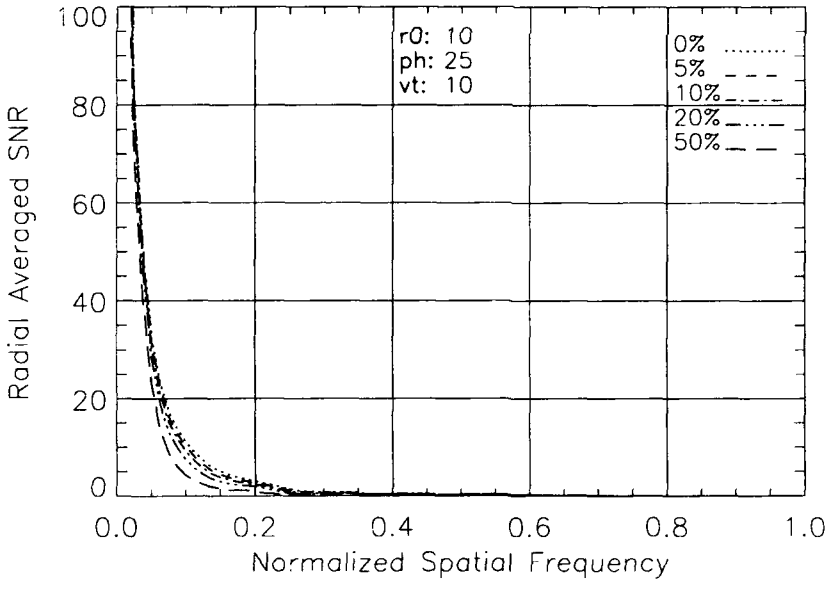

Figure A-10 Misalignment Effects on Radially Avg SNR ($r_0 = 10$, $ph = 25$, $v\tau = 10$)

Additional Failed Actuator Results

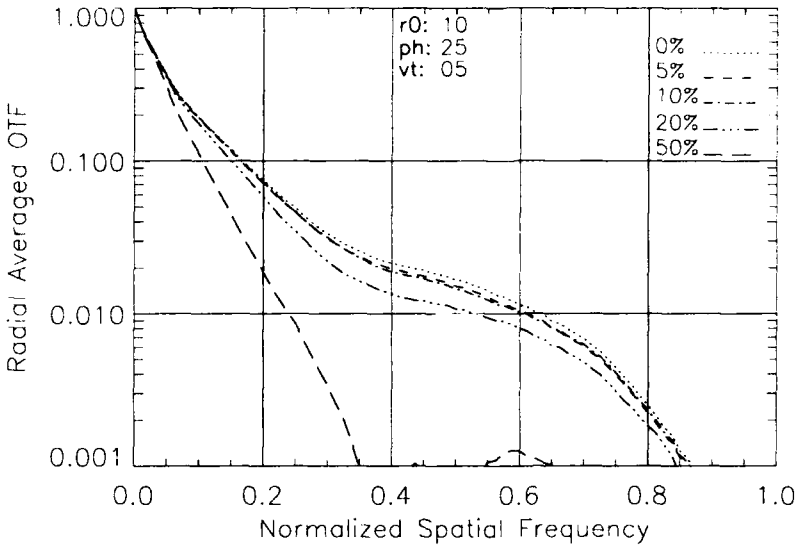

Figure A-11 Failure Effects on Radially Avg OTF ($r_0 = 10$, $ph = 25$, $v\tau = 05$)

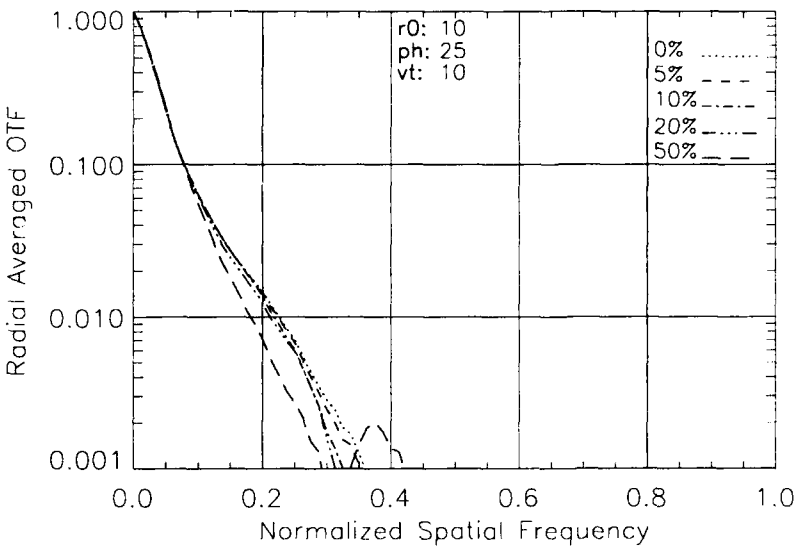

Figure A-12 Failure Effects on Radially Avg OTF ($r_0 = 10$, $ph = 25$, $v\tau = 10$)

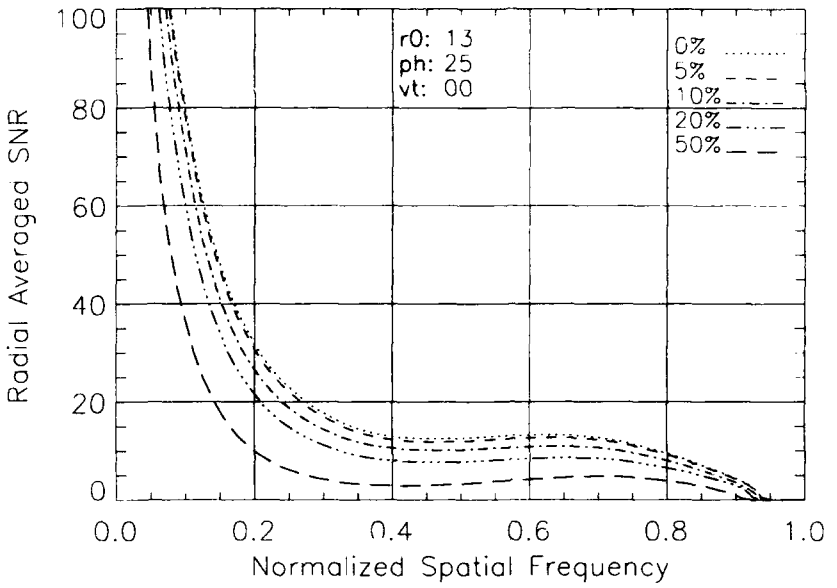

Figure A-13 Failure Effects on Radially Avg SNR ($r_0 = 13$, $ph = 25$, $v\tau = 00$)

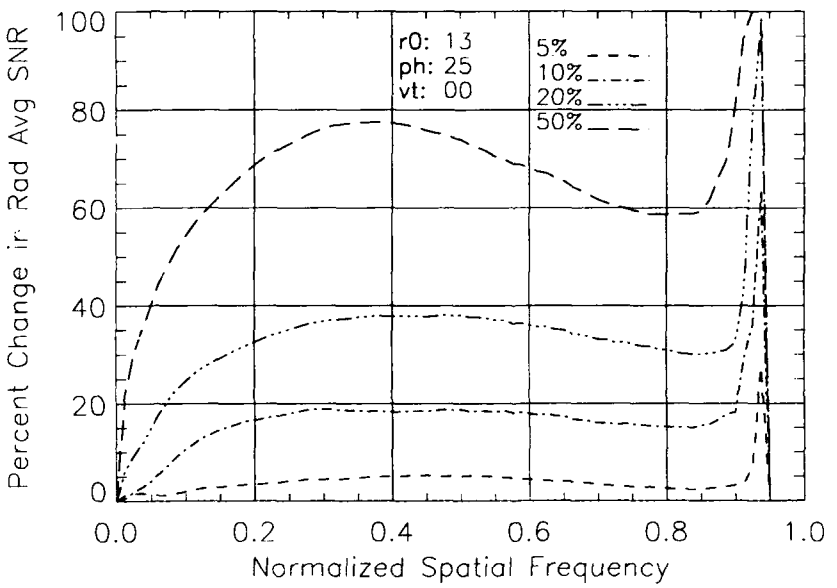

Figure A-14 Failure Effects on Change in Avg SNR ($r_0 = 13$, $ph = 25$, $v\tau = 00$)

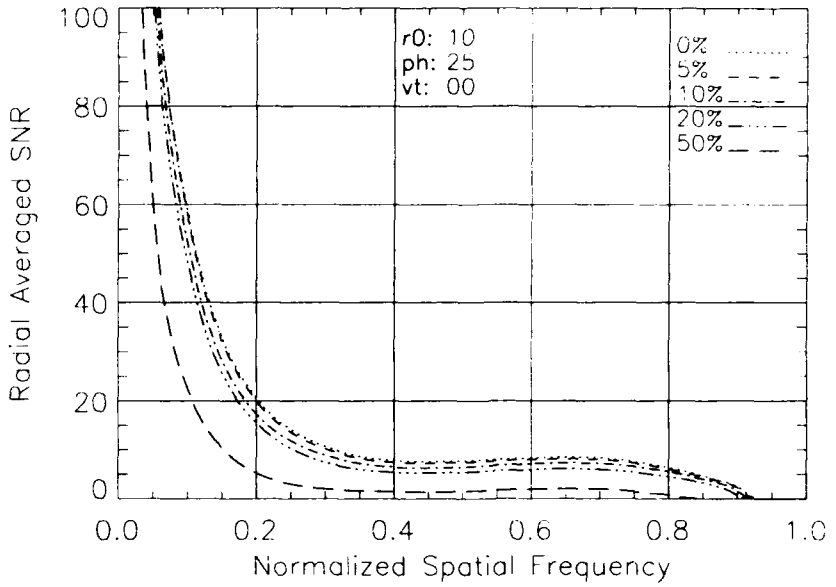

Figure A-15 Failure Effects on Radially Avg SNR ($r_0 = 10$, $ph = 25$, $v\tau = 00$)

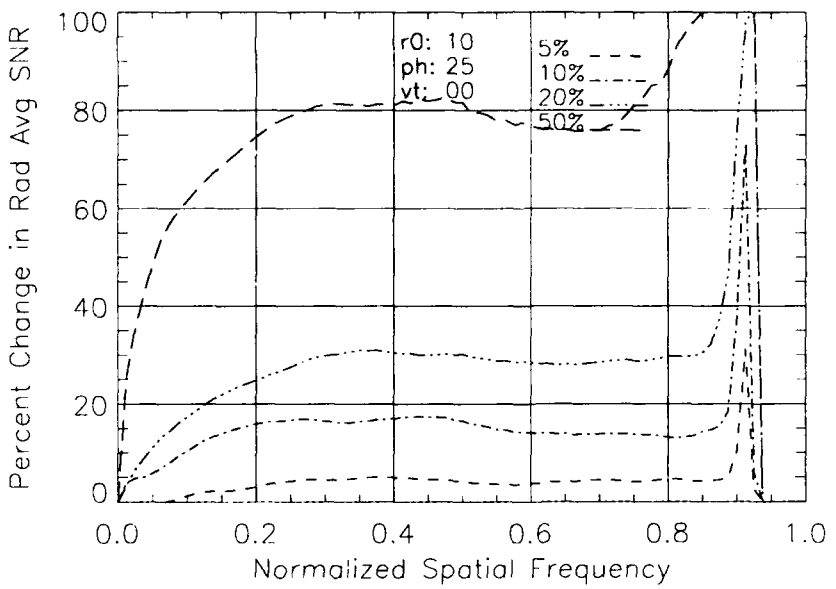

Figure A-16 Failure Effects on Change in Avg SNR ($r_0 = 10$, $ph = 25$, $v\tau = 00$)

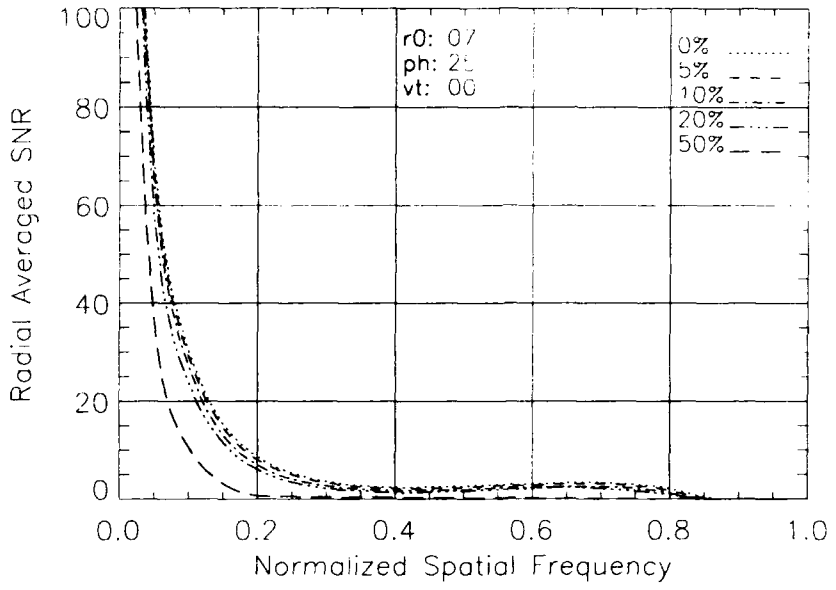

Figure A-17 Failure Effects on Radially Avg SNR ($r_0 = 07$, $ph = 25$, $v\tau = 00$)

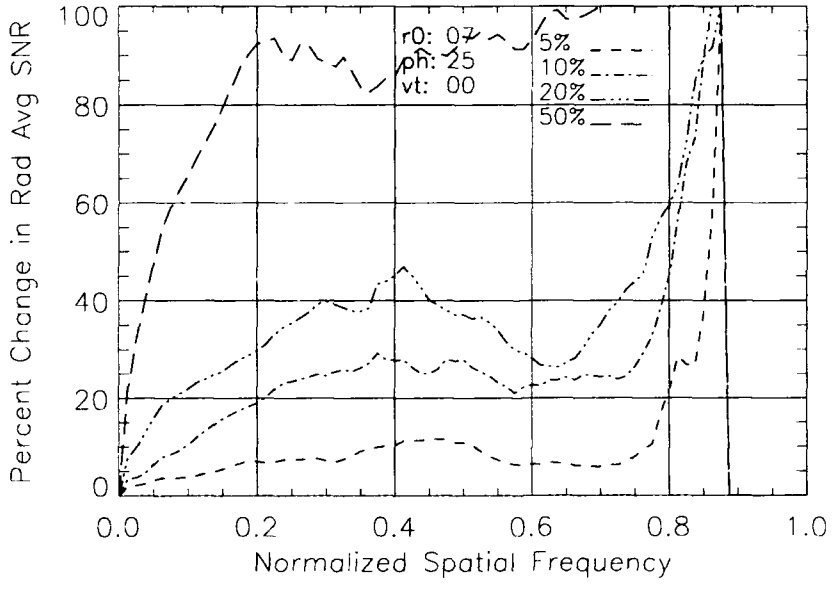

Figure A-18 Failure Effects on Change in Avg SNR ($r_0 = 07$, $ph = 25$, $v\tau = 00$)

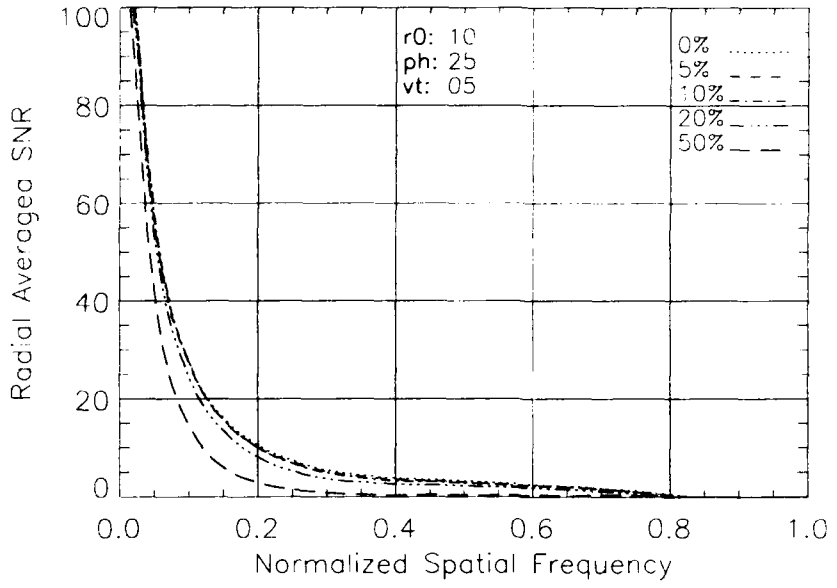

Figure A-19 Failure Effects on Radially Avg SNR ($r_0 = 10$, $ph = 25$, $v\tau = 05$)

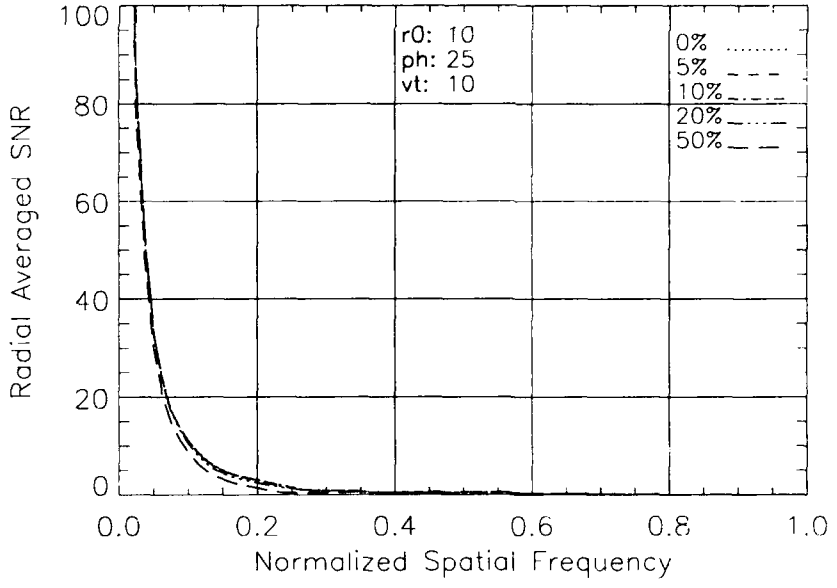

Figure A-20 Failure Effects on Radially Avg SNR ($r_0 = 10$, $ph = 25$, $v\tau = 10$)

BIBLIOGRAPHY

1. Gaffard, J. P. and Boyer, C., "Adaptive Optics for Optimization of Image Resolution," *Applied Optics,* vol 26, pp. 3772-3777 (1987).

2. Goad, L. E., "Performance Scaling Laws for Adaptive Optics Systems," presented April 1993, SPIE conference on adaptive optics, Orlando, FL.

3. Goodman, J., *Statistical Optics, Wiley, New York, 1985.*

4. Hardy, J. W., "Active Optics: A New Technology for the Control of Light," Proc. IEEE vol 66, pp. 651-697 (1978).

5. Nisenson, P. and Barakat, R., "Partial Atmospheric Correction with Adaptive Optics," *Journal of the Optical Society of America,* vol 4, pp. 2249-2253 (1987).

6. Roddier, F., "The Effects of Atmospheric Turbulence in Optical Astronomy," *Progress in Optics XIX.* North-Holland, Amsterdam (1981).

7. Roggemann, M. C., "Limited Degree-of-Freedom Adaptive Optics and Image Reconstruction," *Applied Optics,* vol 30, pp. 4227-4233 (1991).

8. Roggemann, M. C., "Optical Performance of Fully and Partially Compensated Adaptive Optics Systems Using Least-Squares and Minimum Variance Phase Reconstructors," *Computers and Electrical Engineering,* vol 18, pp. 451-456 (1992).

9. Roggemann, M. C. and Meinhardt, J. A., "Image Reconstruction By Means of Wave-front Sensor Measurements in Closed-loop Adaptive-optics Systems," *Journal of the Optical Society of America,* vol 10, No. 9, pp. 1996-2007 (1993).

10. Roggemann, M. C., Tyler, D. W., and Bilmont, M.F., "Linear Reconstruction of Compensated Images: Theory and Experimental Results," *Applied Optics,* vol 31, pp. 7429-7441 (1992).

11. Walner, E. P., "Optimal Wave-front Correction Using Slope Measurements," *Journal of the Optical Society of America,* vol 73, pp. 1771-1776 (1983).

12. Welsh, B. M. and Gardner, C. S., "Performance Analysis of Adaptive-Optics Systems Using Laser Guide Stars and Slope Sensors," *Journal of the Optical Society of America,* vol 6, pp. 1913-1923 (1989).

Vita

Captain Timothy D. Hogan was born on 15 September 1964 in St. Louis, Missouri. He graduated from James B. Conant High School in Hoffman Estates, Illinois in 1982 and attended the University of Illinois, graduating with a Bachelor of Science in Aeronautical and Astronautical Engineering in May 1986. Upon graduation, he successfully completed Undergraduate Space Training at Lowry AFB, Colorado. His first assignment was at Onizuka AFB, California, as assistant project officer for the initial training of Air Force Officers at the Consolidated Space Operations Complex at Falcon AFB, Colorado. In 1988, he was reassigned to the Secretary of the Air Force Special Projects operations unit at Onizuka, where his duties included satellite operations, launch, ground systems engineering support, and emergency reconstitution operations after the Loma Prieta earthquake of 1989. Along with his wife, Mary Ann, and daughters, Kelly Ann and Melissa, he entered the Graduate Space Operations program, Graduate School of Engineering, Air Force Institute of Technology, in May 1992. His follow-on assignment is with the Space Warfare Center (Advanced Programs Division), Air Force Space Command, Falcon AFB, Colorado.

Permanent Address:

c/o Mr. William D. Slaughter
302 Timbercrest Drive
Schaumburg, IL 60193

REPORT DOCUMENTATION PAGE

Form Approved
OMB No. 0704-0188

1. AGENCY USE ONLY (Leave blank)	2. REPORT DATE	3. REPORT TYPE AND DATES COVERED
	December 1993	Master's Thesis

4. TITLE AND SUBTITLE
PERFORMANCE IMPACTS OF ACTUATOR MISALIGNMENTS AND FAILURES IN LARGE-APERTURE ADAPTIVE-OPTIC TELSCOPES

5. FUNDING NUMBERS

6. AUTHOR(S)
Timothy D. Hogan, Captain USAF

7. PERFORMING ORGANIZATION NAME(S) AND ADDRESS(ES)
Air Force Institute of Technology, WPAFB OH 45433-6583

8. PERFORMING ORGANIZATION REPORT NUMBER
AFIT/GSO/ENP/93D-01

9. SPONSORING/MONITORING AGENCY NAME(S) AND ADDRESS(ES)
Capt Brian Berry
Phillips Laboratory/LIMA
3550 Aberdeen SE
Kirtland AFB, NM 87117-5776

10. SPONSORING/MONITORING AGENCY REPORT NUMBER

11. SUPPLEMENTARY NOTES

12a. DISTRIBUTION/AVAILABILITY STATEMENT
Approved for public release; distribution unlimited

12b. DISTRIBUTION CODE

13. ABSTRACT *(Maximum 200 words)*

Large-aperture telescopes require adaptive optics in order to compensate for atmospheric turbulence which would otherwise negate the resolution advantages of using large apertures. This investigation analyzes the impacts of misalignments and failures, in the deformable mirror actuators, upon the performance of such systems. A numerical simulation of a standard adaptive optics system is used to generate characteristic optical transfer function (OTF) and signal-to-noise ratio (SNR) performance metrics. The performance impacts of the misalignments are shown to be dependent upon the Fried parameter (effective telescope diameter), the source object brightness, and the control system time delay. The degree of performance degradation is directly related to the relative value of the Fried parameter to the deformable mirror displacement (misalignment cases) and the effective actuator spacing (actuator failure cases). The results indicate that the impact of misalignments and failures is small when seeing conditions are good or the percentage misalignments and failures are small.

14. SUBJECT TERMS	15. NUMBER OF PAGES
Adaptive Optics, Large-Aperture Telescopes, Atmospheric Compensation	97
	16. PRICE CODE

17. SECURITY CLASSIFICATION OF REPORT	18. SECURITY CLASSIFICATION OF THIS PAGE	19. SECURITY CLASSIFICATION OF ABSTRACT	20. LIMITATION OF ABSTRACT
Unclassified	Unclassified	Unclassified	UL